

# Demonstration of two-dimensional connectivity for a scalable error-corrected ion-trap quantum processor architecture

M. Valentini<sup>\*</sup>,<sup>1</sup> M. W. van Mourik<sup>\*</sup>,<sup>1</sup> F. Butt,<sup>2</sup> J. Wahl,<sup>1,3</sup> M. Dietl,<sup>1,3</sup> M. Pfeifer,<sup>1,3</sup> F. Anmasser,<sup>1,3</sup> Y. Colombe,<sup>3</sup> C. Rössler,<sup>3</sup> P. C. Holz,<sup>4</sup> R. Blatt,<sup>1,4,5</sup> M. Müller,<sup>2</sup> T. Monz,<sup>1,4</sup> and P. Schindler<sup>1</sup>

<sup>1</sup>*Institut für Experimentalphysik, Universität Innsbruck, Technikerstraße 25/4, 6020 Innsbruck, Austria\**

<sup>2</sup>*Institute for Theoretical Nanoelectronics (PGI-2),*

*Forschungszentrum Jülich, 52428 Jülich, Germany*

<sup>3</sup>*Infineon Technologies Austria AG, Siemensstraße 2, 9500, Villach, Austria*

<sup>4</sup>*Alpine Quantum Technologies GmbH, Technikerstraße 17/1, 6020 Innsbruck, Austria*

<sup>5</sup>*Institute for Quantum Optics and Quantum Information, Austrian Academy of Sciences, Technikerstraße 21a, 6020 Innsbruck, Austria*

A major hurdle for building a large-scale quantum computer is to scale up the number of qubits while maintaining connectivity between them. In trapped-ion devices, this connectivity can be provided by physically moving subregisters consisting of a few ions across the processor. The topology of the connectivity is given by the layout of the ion trap where one-dimensional and two-dimensional arrangements are possible. Here, we focus on an architecture based on a rectangular two-dimensional lattice, where each lattice site contains a subregister with a linear string of ions. We refer to this architecture as the Quantum Spring Array (QSA). Subregisters placed in neighboring lattice sites can be coupled by bringing the respective ion strings close to each other while avoiding merging them into a single trapping potential. Control of the separation of subregisters along one axis of the lattice, known as the axial direction, uses quasi-static voltages, while the second axis, the radial, requires control of radio frequency signals. In this work, we investigate key elements of the 2D lattice quantum computation architecture along both axes: We show that the coupling rate between neighboring lattice sites increases with the number of ions per site and the motion of the coupled system can be resilient to noise. The coherence of the coupling is assessed, and an entangled state of qubits in separate trapping regions along the radial axis is demonstrated. Moreover, we demonstrate control over radio frequency signals to adjust radial separation between strings, and thus tune their coupling rate. We further map the 2D lattice architecture to code primitives for fault-tolerant quantum error correction, providing a step towards a quantum processor architecture that is optimized for large-scale fault-tolerant operation.

## I. INTRODUCTION

Ion traps are among the most promising platforms to host quantum computers and simulators. A prominent approach towards scaling ion-based quantum computers to a large numbers of ions is that of the Quantum Charge Coupled Device (QCCD) architecture [1, 2], in which different zones in a microfabricated surface ion trap are used for dedicated tasks such as qubit storage and interaction. In the QCCD architecture, independent trapping regions contain linear strings of ions confined in an individual potential well. Each ion string is considered a quantum subregister and connectivity between qubits in different subregisters requires physical transport of the ions corresponding to the respective subregisters. These reorganization operations require usually splitting and merging of ion crystals [3, 4]. For a scalable system, these one-dimensional trapping regions need to be transferred into a higher-dimensional arrangement of interconnected qubit registers. In the QCCD approach, any higher-dimensional architecture requires additional operations such as ion-crystal rotations [5], and transport operations through junctions [6–8].

Altering the configuration of the subregisters is challenging to implement: during splitting and merging operations, ion strings are subjected to a decreased confining potentials, making them more susceptible to motional excitation due to electrical noise, which limits the performance of subsequent operations [4]. Also, these operations are very sensitive to electric stray fields caused by imperfect trap surfaces. Furthermore, ions that are transported through junctions cannot avoid experiencing an increase in residual RF field [9], and junctions must be carefully designed to limit this type of excursion. These transport operations require a significant portion of the total execution time of a quantum circuit [2, 10]. While operations such as splitting, merging, rotation and transport through junctions have been demonstrated for ion chains with up to four ions [10], the complexity increases for larger numbers of ions per register.

Here we focus on an alternate method to scaling up trapped-ion quantum processors that does not rely on transport of ions between trapping regions: a two-dimensional *lattice* of ion traps [11, 12]. The well-established core building block on each lattice site in this architecture remains a one-dimensional chain of ions. Full ion-to-ion connectivity within such a chain, schematically shown in Fig. 1(a), can be achieved by individually addressed laser pulses. Entanglement within a lattice site

\* These authors contributed equally to this work.

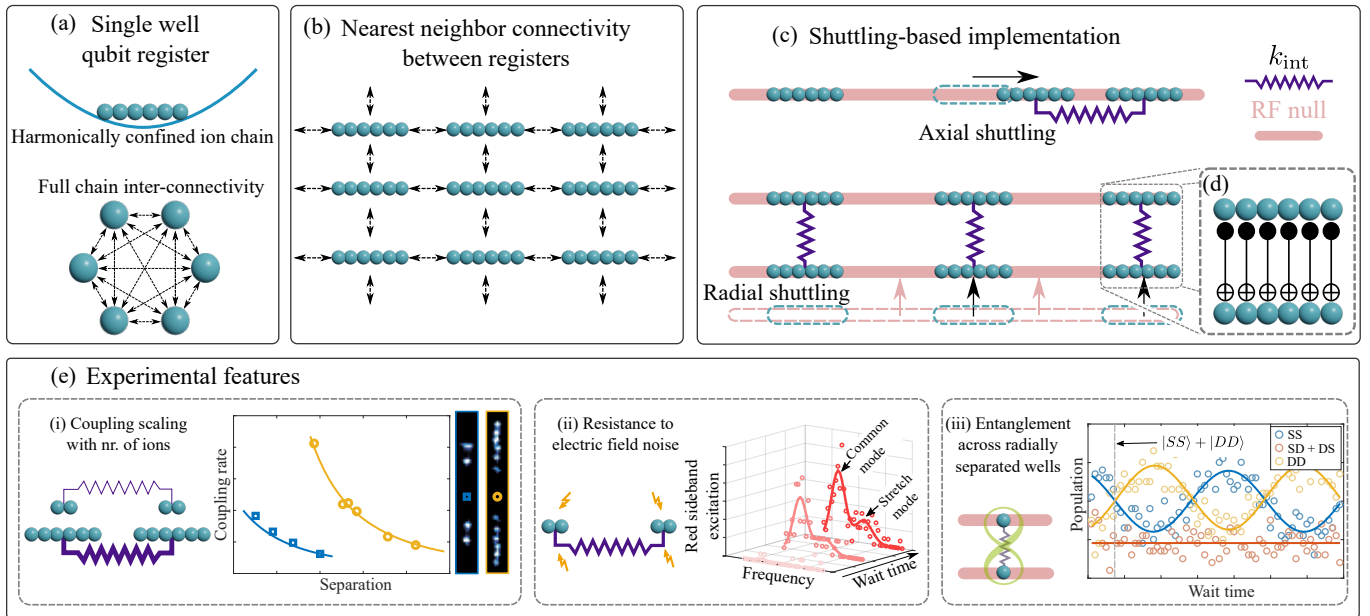


FIG. 1. Overview of the connectivity of the proposed large-scale architecture. (a) A chain of ionic qubits are confined in a single well of an ion trap, with full connectivity between all qubits. (b) Multiple separate trapping regions are distributed along a 2D lattice. Trapping sites have connectivity between nearest neighbors. (c) A shuttling-based approach is used to bring ion chains close enough to couple them, with an interaction constant  $k_{\text{int}}$ . Axial shuttling is achieved by displacing an ion string along a linear trap’s RF null, and radial shuttling is achieved by displacing the RF null itself. When coupled, all-to-all connectivity between ions in separate strings is enabled. In particular, as depicted in (d) transversal operations between pairs of ions are made possible. (e) Experimental highlights discussed in this work include: (i) the favorable scaling of coupling rate with number of ions, (ii) the resistance to electric field noise of the double well stretch mode of the coupled-ion system compared to the common mode, and (iii) generation of an entangled state,  $|SS\rangle + |DD\rangle$ , in radially separated ions, mediated by an oscillatory exchange of motion between two separated wells.

is mediated by the chain’s common mode of motion. The quantum processor is then built up from a physical 2D lattice configuration of these chains [13, 14]. Connectivity between neighboring lattice sites, and thus subregisters, is achieved through Coulomb interaction between the individual ion chains, as shown in Fig. 1(b). This level of connectivity permits a broad class of algorithms, but avoids the complications involved in multi-ion splitting, merging, and junction transport. We refer to this coupled-lattice architecture as a Quantum Spring Array (QSA).

In the QSA architecture, the default configuration features a distance between ion chains that is large enough such that coupling between them is negligible. Interaction between chains is enabled by moving two chains of ions close to each other, though without merging them into a single potential well. Due to the geometrical configuration of linear ion traps, the two orthogonal directions of shuttling require two different types of control. As schematically depicted in Fig. 1(c), these directions are denoted as axial and radial, referring to their orientation with respect to the 1D ion string.

Coherent coupling between subregisters is a crucial element of scalable quantum information processing. The QSA architecture avoids the necessity of splitting and merging of ion chains, and shuttling through junctions.

This also relaxes the constraint that the subregisters are limited to a small numbers of ions. In fact, in the QSA approach, larger register sizes are advantageous, as it enhances coupling between neighbors. In this work, we experimentally demonstrate these advantages by investigating interaction between ion chains along both the axial and radial directions. Axial coupling and also entanglement between ions in different potential wells has previously been observed [15–17]. Here we investigate the increased coupling rate that emerges from large ion crystals and show that the coupled ion strings provide usable motional modes that are resilient to electric field noise. Our work furthermore presents the first realization of coherent coupling and entanglement in radially separated linear traps, signifying an important step towards control of qubits in two dimensions. Finally, we show how the QSA architecture is ideally suited to host fault-tolerant quantum error correction protocols, thereby providing a first step towards a trapped-ion based, optimized fault-tolerant quantum computing architecture.

Axial and radial coupling are demonstrated using two separate types of surface traps, each with an electrode layout specifically suited for one of the two schemes. All traps are operated in a cryogenic environment. The experiments involve  $^{40}\text{Ca}^+$  ions placed in a double-well trapping potential, ranging from one to six ions per well.

Detection of the electronic states of ions or spatial information is performed by fluorescence detection using either an Electron-multiplying CCD (EMCCD) camera or photomultiplier tube (PMT).

Our results are summarized as follows: we first revisit the theory of well-to-well coupling, and numerically calculate the coupling rate between chains of ions. This calculation is used to show a beneficial scaling of coupling rate with the number of ions per chain for axial coupling (Section II). Our numerical calculations are experimentally confirmed by measuring both the axial and radial coupling rates for various numbers of ions per potential well (see Fig. 1(e)(i), further detailed in Sections III A and IV A). Coupled ion strings are subsequently controlled to demonstrate that motional excitation can be coherently exchanged between the two potential wells, a requirement for generating entanglement. We present a first demonstration of entanglement of radially separated ions (Fig. 1(e)(iii) and Section IV A). We investigate a unique feature that different modes of the coupled system exhibit notably different heating rates under the influence of electrode voltage noise (Fig. 1(e)(ii)). This allows the fidelity of entangling gates to be resistant to motional decoherence, even for large numbers of ions per well. On the route towards scalable control of 2D trap arrays, we demonstrate that through control of RF voltages, we are able to adjust the separation, and thus coupling rate, between neighboring ion strings (Section V).

In Section VI, we explore avenues to harness the potential of the QSA architecture for scalable quantum computation, specifically within the context of quantum error correction (QEC). Here, the overhead of shuttling operations can be minimized by matching the QEC code to the given architecture. As an example, we investigate mapping of concatenated quantum codes onto the QSA architecture, providing a pathway to error-corrected and universal logical quantum computation.

## II. THEORY: INTERACTION BETWEEN SEPARATED ION CHAINS

Trapped ion qubits are usually stored in subregisters comprising of one-dimensional ion chains, whose axis is aligned with the so-called RF-null [18, 19]. This region coincides with a minimum in the effective trapping potential experienced by ions in the radio frequency field created by the trap electrodes. Ion transport along the one-dimensional RF-null is referred to as axial shuttling. This can be achieved through control of the static trapping fields which are known as DC potentials. While some deviation of the ions' positions from the RF-null is permissible [5], excursions of several micrometers are detrimental to the performance of ions as a string of qubits, since the larger amplitude of the RF-field destabilizes ion chains [20, 21]. Thus, two-dimensional ion transport requires a second distinct strategy of manipulation of trapping potentials: We implement radial shuttling by

altering the position of the RF-null itself. The transport strategies are schematically depicted in Fig. 2(a).

In both axial and radial transport strategies, the aim is to bring two (pseudo)potential minima, each containing a group of ions, towards each other, though without merging them into a single well. This allows separated ion chains to experience an enhanced coupling through Coulomb interaction, enabling entangling gate operations to be performed. In this section, we describe the formalism for coupling of ion chains in separate potential wells as a function of the spatial distribution and charge of the ion chains, and orientation of their modes of oscillation.

### A. Coupling rate of separated charges

An approximate way to model the coupling of separated ion chains is to approximate the interaction potential with that of a dipole-dipole interaction of point charges [15, 16]. The interaction potential is given by

$$V_{\text{int}} = \frac{Q_1 Q_2}{4\pi\epsilon_0} \frac{\vec{r}_1 \cdot \vec{r}_2 - 3(\vec{r}_1 \cdot \hat{e}_d)(\vec{r}_2 \cdot \hat{e}_d)}{d^3} \quad (1)$$

with  $Q_{\{1,2\}}$  the total charge in each of the two wells,  $\epsilon_0$  the dielectric constant in vacuum, and  $\vec{r}_{\{1,2\}}$  the displacement of the charges from their equilibrium positions. Here,  $d$  is the distance between charges, and  $\hat{e}_d$  the unit vector in the direction of separation.

In this work we consider the well-to-well interaction of ions through their *axial* motion, the mode of motion that aligns with the axis of the RF-null(s). Here, we choose to define the axial direction to lie along the  $z$ -axis. We choose this mode instead of radial modes of motion, since it typically has longer coherence times as it is defined by static voltages, and has a stronger coupling to laser fields than the radial modes. The stronger coupling is due to the lower Lamb-Dicke parameter due to lower trap frequency. For the trap geometries presented in this work, the axial modes of each well are parallel, such that  $\vec{r}_1 \cdot \vec{r}_2 = |\vec{r}_1||\vec{r}_2|$ . The axis of well-to-well separation, given by  $\hat{e}_d$ , is parallel with the axial modes in axial shuttling, and is perpendicular with the axial modes in radial shuttling. In other words, the interaction is represented by dipole-dipole coupling with dipoles oscillating either in the direction of separation, or perpendicular to it. These directions of coupling, schematically shown in Fig. 2(b) and (c), are referred to as axial and radial coupling, respectively. The second fraction in Eq. 1 reduces to  $\kappa|\vec{r}_1||\vec{r}_2|/d^3$ , with  $\kappa = -2$  for axial coupling and  $\kappa = 1$  for radial coupling. The interaction potential can thus be written as  $V_{\text{int}} = k_{\text{int}}|r_1||r_2|$ , where  $k_{\text{int}}$  is an interaction constant analogous to a spring constant, given by

$$k_{\text{int}} = \kappa \frac{Q_1 Q_2}{4\pi\epsilon_0 d^3} \quad (2)$$

The motion of a collection of  $n$  trapped ions with mass  $m$  and charge  $q$  in a single potential well can be expressed

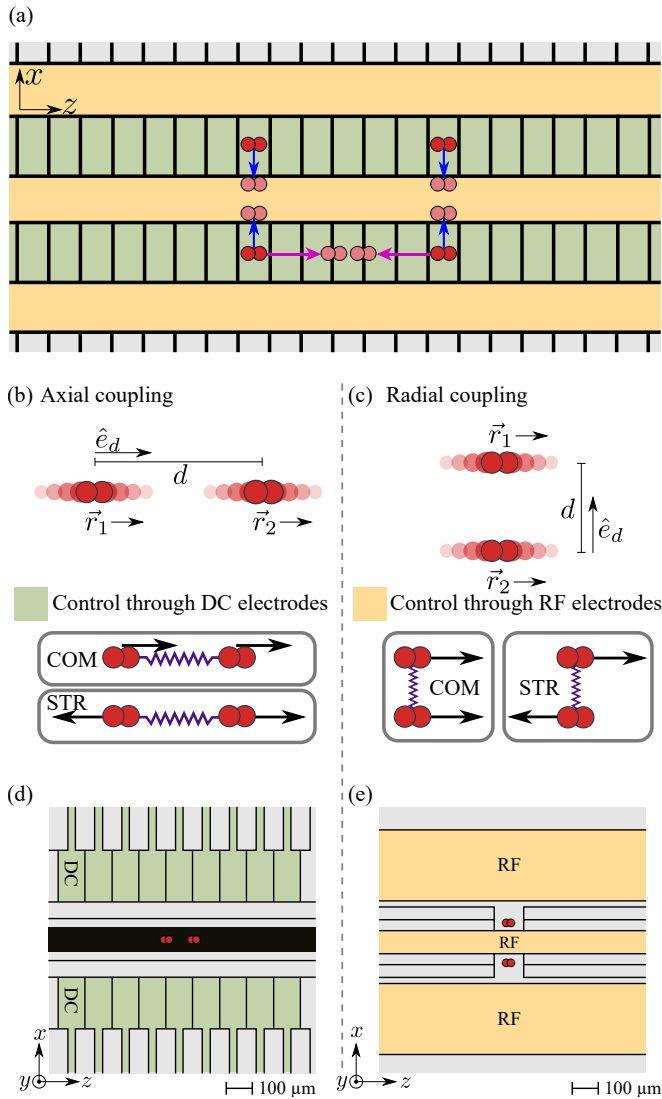


FIG. 2. (a) Schematic depiction of an ion trap layout that enables axial (purple arrows) and radial (blue arrows) shuttling to adjust the separation between trapping sites in two dimensions. The direction of separation  $\hat{e}_d$  lies along the (b) axial and (c) radial direction with respect to the ion chain's axial mode of oscillation leading to axial and radial mode coupling, respectively. In both cases, coupled ions exhibit shared modes of motion, and can oscillate in phase (COM - common), or out of phase (STR - stretch). In this work, the two means of coupling are investigated in separate ion traps, whose layouts are shown in (d) and (e).

as that of a harmonic oscillator. The confining potential's curvature  $\phi_z$  defines the uncoupled common oscillation frequency along the axial direction as  $\omega_z = \sqrt{q\phi_z/m}$ . Thus, two chains of ions trapped in separate wells can be described as two coupled harmonic oscillators, with an interaction potential given by Eq. (1).

We consider the case that the collection of ions in both wells contain the same number  $n$  of identical ions, and thus have the same overall charge  $Q = nq$  and mass  $nm$ .

Furthermore, we assume the axial curvature  $\phi_z$  to be identical in both wells. Neglecting internal degrees of freedom within individual ion chains, the total potential energy relevant to the system's axial modes of motion is given by  $V_z = \phi_z(r_{z,1}^2 + r_{z,2}^2)/2 + V_{\text{int}}$ , where  $r_{z,1}$  and  $r_{z,2}$  represent the axial displacement of the first and second chain. Mode analysis in the basis  $(r_{z,1}, r_{z,2})$  results in two distinct eigenmodes,  $(1, 1)$  and  $(1, -1)$  in which ions in the separate wells oscillate in and out of phase with each other, respectively. These modes are schematically depicted in Fig. 2(b) and (c). In both cases, both chains of ions equally contribute to the mode, making these modes ideal channels to transfer quantum information between wells. The frequencies of these modes are given by

$$\omega_{\text{com,str}} = \sqrt{\omega_z^2 \pm \frac{k_{\text{int}}}{nm}} \quad (3)$$

with a '+' for the in-phase (common, COM) mode, and a '-' for the out-of-phase (stretch, STR) mode. The difference in frequency of these modes,  $\Omega_c = |\omega_{\text{com}} - \omega_{\text{str}}|$ , is commonly referred to as the coupling rate. For a small interaction potential,  $|k_{\text{int}}| \ll mn\omega_z^2$ , the coupling rate can be expressed as [15, 16]

$$\Omega_c = \frac{|\kappa|nq^2}{4\pi\epsilon_0 m\omega_z d^3}. \quad (4)$$

The coupling rate presents an upper bound to the rate at which motional information can be exchanged between wells, and is in practice an upper bound for the rate at which entanglement between wells can be achieved.

The model of Eq. 4 predicts a linear increase in coupling with an increasing number of ions  $n$ . Entangling operations therefore benefit from being implemented on larger registers of qubits, since the duration of the operation decreases, reducing computation time and susceptibility to decoherence. However, the presented model for coupling strength has neglected the spatial extent of the ion chains and is only exactly valid for one ion per well. Numerical methods, outlined below, are required to obtain coupling rates for arbitrary numbers of ions per well.

## B. Coupling rates of ion strings

A 2D array of trapped ion chains requires a trapping potential that is periodic in two dimensions. We begin our analysis with a simpler model, where we consider a double-well potential, along either the axial or radial axis. We use the coordinate system  $\{x, y, z\}$ , as depicted in Fig. 2(d) and (e), and denote positions as  $\vec{r} = (r_x, r_y, r_z)$ . The lowest-order polynomial representation of a symmetric double-well potential that confines ion chains in two separated trapping regions in three dimensions is given by

$$V_{\text{ax}} = \alpha r_z^2 + \beta r_z^4 + \frac{1}{2}\phi_x r_x^2 + \frac{1}{2}\phi_y r_y^2 \quad (5)$$

for axial coupling as in Fig. 2(b), and

$$V_{\text{rad}} = \alpha r_x^2 + \beta r_x^4 + \frac{1}{2} \phi_y r_y^2 + \frac{1}{2} \phi_z r_z^2 \quad (6)$$

for radial coupling as in Fig. 2(c). In both cases,  $\alpha$  and  $\beta$  represent coefficients that scale with the second and fourth order curvatures along the double-well axis, and  $\phi_{\{x,y,z\}}$  are second order curvatures along the remaining axes. The parameters  $\alpha$  and  $\beta$  define a double well that confines positively charged particles when  $\beta > 0$  and  $\alpha < 0$ . The separation of the wells is uniquely defined by these parameters, as  $d = \sqrt{-2\alpha/\beta}$ , and each well has a local potential curvature coefficient given by  $\alpha_w = -2\alpha$ . The local curvature sets the secular frequency  $\omega$  of an ion trapped along the axis of the double well,  $\omega = \sqrt{2q\alpha_w/m}$ , though it should be noted that if the well contains multiple ions, the motional frequency can deviate from this value due to the spatial extent of the ion crystal in an anharmonic potential. In our surface traps, we can independently control the curvature parameters  $\alpha$ ,  $\beta$ , and  $\phi_{\{x,y,z\}}$  through a predetermined and calibrated set of DC and RF electrode voltages.

To determine the coupling rate between ions in separate wells, we first determine the equilibrium positions of all ions in both strings,  $\vec{r}_{\text{min}}^{(i)}$ . These positions are found by numerically minimizing the system's total potential energy  $V_T$ , given by

$$V_T = \sum_i \left( V_{\text{ax/rad}}(\vec{r}_{\text{min}}^{(i)}) + \frac{1}{2} \sum_{j \neq i} V_{\text{Coul}}(\vec{r}_{\text{min}}^{(i)}, \vec{r}_{\text{min}}^{(j)}) \right) \quad (7)$$

with  $V_{\text{Coul}}(\vec{r}_{\text{min}}^{(i)}, \vec{r}_{\text{min}}^{(j)})$  the Coulomb interaction between ions  $i$  and  $j$ . Mode vectors  $\vec{v}_l$  of modes indexed  $l$  are found by calculating the eigenvectors of the mass-corrected Hessian  $H$  of  $V_T$ , with terms

$$H_{i,j} = \frac{1}{m} \left. \frac{\delta^2 V_T}{\delta r_k^{(i)} \delta r_k^{(j)}} \right|_{\vec{r}_{\text{min}}}, \quad (8)$$

for all ions  $i$  in all directions  $k \in \{x, y, z\}$ . The square-roots of the eigenvalues of  $H$  are the mode frequencies,  $\omega_l$ . We obtain, in particular, the mode frequencies  $\omega_{\text{com}}$  and  $\omega_{\text{str}}$  that correspond to eigenvectors in which the two ion chains collectively oscillate in phase and out of phase with each other. A feature of using these modes for ion coupling is the simplification of the overall mode structure of two separated ion strings, compared with that of joining two ion strings together into a single well. Only two modes of oscillation need to be considered, which are conceptually similar to the in-phase and out-of-phase modes of a system of two co-trapped ions.

The coupling rate  $\Omega_c$  is given by the difference of these in-phase and out-of-phase frequencies,  $|\omega_{\text{str}} - \omega_{\text{com}}|$ . An effective interaction constant  $k_{\text{int}}$  between the chains can be obtained from the inverse of Eq. 3,

$$k_{\text{int}} = \frac{1}{2} nm \Omega_c \sqrt{4\omega_z^2 - \Omega_c^2} \quad (9)$$

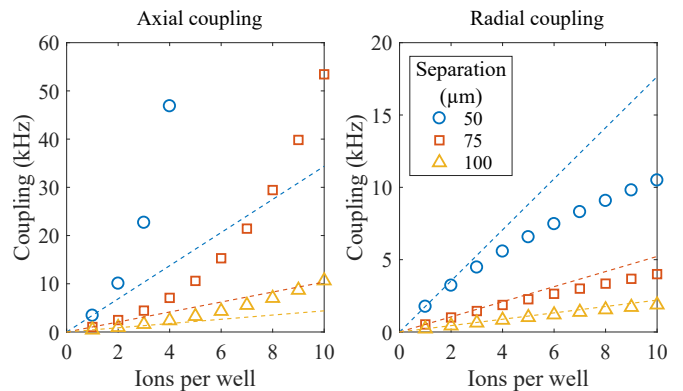


FIG. 3. Simulated coupling rate as a function of number of ions per well, for various separations of harmonic trap sites. The common mode frequency of the individual wells is set to 400 kHz for each point. If the axis of separation is along the ion chains' axial direction (axial coupling, left), the coupling scales almost quadratically with number of ions, while for a separation along the radial direction (radial coupling, right) the scaling is sub-linear. Dashed lines are the coupling rates predicted from the point-charge model (Eq. 4), which has a linear scaling with number of ions.

where  $\omega_z = \sqrt{-4q\alpha/m}$  for axial coupling and  $\omega_z = \sqrt{q\phi_z/m}$  for radial coupling.

Fig. 3 displays coupling rates using the numerical approach, calculated as a function of number of ions per well for various well-to-well separations, for coupling along the axial and radial directions. The curvatures  $\alpha$ ,  $\beta$ , and  $\phi_{x,y,z}$  are set to ensure chains of ions align along the  $z$ -axis, such as depicted in Figs. 2(b) and (c). Furthermore, in each configuration, the potential curvatures are set to produce an uncoupled axial common mode frequency of each ion chain of 400 kHz.

The numerical calculations presented in Fig. 3 show that axial coupling benefits from a super-linear scaling between number of ions and coupling, a notable increase with respect to the predicted linear scaling of the point-charge model. This favorable scaling allows for coupling of larger registers of qubits in separate wells at time scales similar to that which can be achieved for fully merged and split crystals, while avoiding the complications involved in such operations. For radial coupling, on the other hand, the scaling is sub-linear. Regardless, given that there is as of yet no viable splitting-and-merging approach to radial coupling, radial well-to-well coupling presents a feasible approach towards control of 2D qubit lattices.

The potentials given by Eqs. 5 and 6 are experimentally realized with a set of DC and RF voltages that are predetermined using electrostatic simulations of our trap models. In practice, trap potentials will deviate from desired potentials due to limits in numeral precision in the electrostatic simulation, tolerances in the fabrication of the traps, and unaccounted stray fields. The most notable effect of this deviation is that the axial field cur-

vatures at the position of the two ion chains may not be equal. As a result the motional frequencies of uncoupled chains,  $\omega_{z,1}$  and  $\omega_{z,2}$ , are not necessarily on resonance. The resulting mode frequencies deviate from those given by Eq. 3, and are instead given by

$$\omega_{\pm} = \sqrt{\frac{\Delta\omega^2}{4} + \omega_m^2} \pm \sqrt{\frac{k_{\text{int}}^2}{n^2 m^2} + \Delta\omega^2 \omega_m^2}, \quad (10)$$

in which we have used the difference frequency  $\Delta\omega = \omega_{z,2} - \omega_{z,1}$  and the mean frequency  $\omega_m = (\omega_{z,1} + \omega_{z,2})/2$ . The modes of motion are given by

$$\frac{1}{\sqrt{1 + (\sqrt{1 + \chi^2} \mp \chi)^2}} \left( -\chi \pm \sqrt{1 + \chi^2}, 1 \right), \quad (11)$$

with  $\chi = nm\omega_m\Delta\omega/k_{\text{int}}$ .

For a large difference in frequencies of the two harmonic oscillators,  $\Delta\omega \gg k_{\text{int}}/(nm\omega_m)$ , (i.e.,  $\lim_{\chi \rightarrow \infty}$ ) eigenmodes are  $(1, 0)$  and  $(0, 1)$  and thus the wells are not coupled. When the harmonic oscillators are tuned into resonance,  $\Delta\omega = 0$  (i.e.,  $\chi \rightarrow 0$ ), the two coupled modes,  $(1, 1)/\sqrt{2}$  and  $(1, -1)/\sqrt{2}$  at frequencies  $\omega_{\text{com}}$  and  $\omega_{\text{str}}$  emerge.

The frequency response of  $\omega_+$  and  $\omega_-$  as a function of  $\Delta\omega$  exhibits an avoided crossing around  $\Delta\omega = 0$ . The avoided crossing is a useful experimental feature, as it allows us to accurately determine the coupling rate, by measuring the motional frequencies  $\omega_+$  and  $\omega_-$  of the double-well system while varying  $\Delta\omega$ . The coupling rate at resonance is given by the minimum value of  $|\omega_+ - \omega_-|$ .

### C. Mode heating of coupled ion strings

Anomalous heating is a common affliction in ion traps, and is exacerbated in *surface* traps, as ions are in relatively close proximity to electrodes which may carry voltage noise [22–26]. The rate of excitation of an individual mode is dependent on the projection of the noisy field at the position of the ions onto the mode’s eigenvector.

As described in Section II A, the coupled ion strings exhibit an in-phase (common) and out-of phase (stretch) mode of oscillation. The common mode, with mode vector  $(1, 1)$  can be excited if field-noise is homogeneous over the two ion positions. The stretch mode with mode vector  $(1, -1)$ , on the other hand, cannot be excited with a homogeneous field and only responds to unequal fields at the ion positions. Since the ion-electrode distance is typically larger than the separation between the coupled ion-chains, the electric field noise is predominantly homogeneous. The stretch mode is therefore less susceptible to mode heating, making it a good choice for use in entangling operations. The fact that the stretch mode (and other higher-order modes) have lower heating rates is well-known for chains of ions in a single well [27]. However, for single-well chains of more than 2 ions, ions participate unequally in such modes, making them less

suitable for entangling operations. In the double-well approach, the two chains of ions equally participate in the stretch mode, and furthermore benefit from the same low motional frequency as their bare common modes.

In the following, we present a model for estimating mode heating due to voltage noise. We first determine the ions’ equilibrium positions for a known single- or double-well potential, following the procedure outlined in Section II B. We then determine the axial electric field component  $E_k(\vec{r}_{\text{min}}^{(i)})$  per volt for each independent DC electrode  $k$ , analyzed at each ion position. This field is obtained using finite-element electrostatic field simulations. We cast this field at multiple ion positions into the vector  $\vec{E}_k$ . The contribution of a noisy electric field to mode heating is determined by its projection onto that mode, given by  $\vec{E}_{k,\parallel n} = (\vec{E}_k \cdot \vec{v}_n)\vec{v}_n$ . The heating rate  $\Gamma_{n,k}$  of a mode  $n$  due to electrode  $k$  is proportional to the square of the total force applied to the chain by  $\vec{E}_{k,\parallel n}$ , given by  $(q \sum_i |E_{k,\parallel n}^{(i)}|)^2$ , and inversely proportional with the mass of the chain, [22]. We thus have a prediction for heating rate per voltage noise, for each electrode, for a given trap geometry. The total heating rate of mode  $n$  is the sum of that of each electrode,  $\Gamma_n = \sum_k \Gamma_{n,k}$ . We experimentally investigate heating of coupled ion strings due to electric field noise in Sections III C and IV C.

## III. WELL-TO-WELL COUPLING IN THE AXIAL DIRECTION

In this section, we experimentally investigate well-to-well coupling of ion strings along the axial direction. We show how the coupling rate scales with number of ions per well, observe coherent exchange of motion between wells, and investigate sensitivity of the double-well system to electric field noise. For these experiments, the slotted surface trap schematically shown in Fig. 2(d) is used. A set of static voltages on electrodes that flank the trapping region (marked ‘DC’ in Fig. 2(d)) are used to generate a symmetric double well potential along the  $z$ -axis, given by the quadratic and quartic potential terms in Eq. 5,  $\alpha$  and  $\beta$ .

### A. Coupling rate

The coupling rate between ion chains in separate wells is obtained by experimentally determining the mode frequencies of the sets of ions in individual wells. As described in Section II B, these frequencies,  $\omega_+$  and  $\omega_-$ , exhibit an avoided crossing when scanned across resonance, and the minimum frequency difference determines the coupling rate  $\Omega_c$ .

The motional frequencies of ions in both wells can be tuned by introducing a homogeneous field  $E_z$  in the axial direction, which alters the double well potential to  $V_{\text{ax}} = -E_z r_z + \alpha r_z^2 + \beta r_z^4$  (neglecting field components in the  $x$

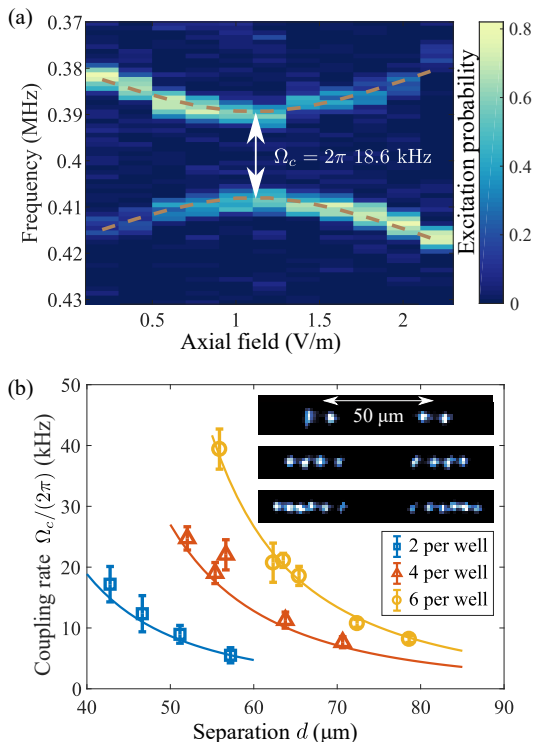


FIG. 4. (a) Example of the avoided crossing in the coupling rate measurement for  $n = 6$  ions per well. (b) Measured coupling rate for various numbers  $n$  of ions per well, and various separations. Lines are simulated values. Insets display chains of ions detected with an EMCCD camera.

and  $y$  directions). As with the double-well potential, this additional field is produced by adding a predetermined and calibrated set of voltages to the trap electrodes. For harmonically confined ions, such a field would ordinarily not change the motional frequency. However, since the local trapping potential around each well is anharmonic, this field generates a change in motional frequencies of approximately equal magnitude but opposite sign in the two wells. Applying a homogeneous field therefore allows us to bring the two motional frequencies in and out of resonance, and is by approximation linearly proportional to scanning  $\Delta\omega$  in Eqs. 10 and 11, while keeping the mean frequency  $\omega_m$  constant. We can then deduce the coupling rate by observing the magnitude of the avoided crossing at  $\Delta\omega = 0$ .

Fig. 4(a) displays an example of an avoided crossing measurement, where the color mapping represents the mean excitation of all ions from only one of the two wells. The two wells each contain  $n = 6$  ions, and are separated by  $d = 65 \mu\text{m}$ . The motional frequencies of the chains are about 400 kHz. We vary both the laser frequency (vertical axis, displayed as detuning from the carrier frequency) and the applied field (horizontal axis). The plot shows both how the detuning between wells,  $\Delta\omega$ , affects the motional frequencies as given by Eq. 10 and how it affects the magnitude of participation in each mode, as given by Eq. 11.

The magnitude of the applied stray field at which the avoided crossing occurs,  $\approx 1.11 \text{ V m}^{-1}$ , is not zero. This discrepancy is caused by stray fields from patch potentials on the trap surface, and limited numerical precision when calculating voltages to generate the double-well potential.

Motional frequencies for each axial field setting in Fig. 4(a) are obtained by fitting the data to a Gaussian function. The measured frequencies are compared to a model function based on Eq. 10, given by

$$\omega_{\pm} = a\sqrt{(\gamma - d)^2/4 + b} \pm \sqrt{c^2 + b(\gamma - d)^2}, \quad (12)$$

with  $a \dots d$  fit parameters, and  $\gamma$  the applied field. The coupling frequency  $\Omega_c$  is inferred from a least-squares regression between the measured data and the model, with

$$\Omega_c = \omega_+(\gamma = d) - \omega_-(\gamma = d) = a(\sqrt{b+c} - \sqrt{b-c}). \quad (13)$$

In the example of Fig. 4(a), we find  $\Omega_c = 2\pi \cdot 18(2)$  kHz.

Fig. 4(b) displays the measured coupling rate for multiple avoided crossing scans. Here, we vary the number of ions per well ( $n = 2, 4$  and  $6$ ), and the separation between wells. The mean motional frequency of the wells  $\omega_m$  has been fixed for all configurations to be  $2\pi \cdot 400$  kHz. Note that since the common mode frequency in an anharmonic potential is dependent on the number of ions, the double-well potential parameters  $\alpha$  and  $\beta$  must be adjusted as a function of ion number to counteract this dependence.

The solid lines in Fig 4(b) are numerically calculated values for the coupling rate. No free parameters are used in obtaining simulated values, solely the well-to-well separation and the mean common mode frequency. With an R-square value of 0.95, the simulated and measured values are in excellent agreement.

At a separation of  $56 \mu\text{m}$ , we measure a coupling rate of  $2\pi \cdot 39(3)$  kHz between two wells containing 6 ions each. In contrast to the dipole-dipole interaction model which predicts a linear scaling with number of ions, this is a sixteen-fold, as opposed to six-fold, improvement over the predicted  $2\pi \cdot 2.5$  kHz coupling that would be achieved for a configuration with 1 ion per well with the same separation and motional frequency.

## B. Phonon exchange

A prerequisite for coherent control of qubits in separate wells, such as entangling operations, is that motional excitation can be coherently exchanged between the two wells. This section details the experimental observation of coherent exchange of motional excitation of ion strings in separate wells.

As described in Section II, we consider the motion characterized by the displacement of the string of ions in each well,  $\vec{r} = (r_{z,1}, r_{z,2})$ . When on resonance, eigenmodes of oscillation are given by  $\vec{v}_{\text{com}} = 1/\sqrt{2}(1, 1)$  and

$\vec{v}_{\text{str}} = 1/\sqrt{2}(1, -1)$ , and have frequencies separated by the coupling rate,  $\Omega_c$ . A displacement of ions in the first well,  $r_{z,1} = \lambda$  is written in terms of eigenmodes as  $\lambda/\sqrt{2}(\vec{v}_{\text{com}} + \vec{v}_{\text{str}})$ , which has a free evolution given by

$$\vec{r} = \frac{\lambda}{\sqrt{2}} [\sin((\omega_m - \Omega_c/2)t) \vec{v}_{\text{com}} + \sin((\omega_m + \Omega_c/2)t) \vec{v}_{\text{str}}]. \quad (14)$$

Reformulation with trigonometric identities results in

$$\vec{r} = \lambda \left( \cos\left(\frac{\Omega_c t}{2}\right) \sin(\omega_m t), -\sin\left(\frac{\Omega_c t}{2}\right) \cos(\omega_m t) \right) \quad (15)$$

from which we see both sets of ions oscillating at the trap frequency  $\omega_m$ , though with an amplitude modulated at a rate  $\Omega_c/2$ . An excitation applied to ion chain 1 is therefore fully transferred to ion chain 2 after a time  $t_{\text{exc}} = \pi/\Omega_c$ , and returned at  $2t_{\text{exc}}$ . A similar treatment of exchange of motional excitation can be made with a quantum mechanical description of the coupled harmonic oscillator system [17]. In such a system, it can be shown that the mean local phonon number oscillates between wells.

We directly observe this exchange of excitation in our experiment. We use a system of two ions per well, separated by  $58 \mu\text{m}$ , at a motional frequency of  $460 \text{ kHz}$ . We measure a coupling rate of  $2\pi \ 5 \text{ kHz}$  from the avoided crossing in Fig. 4. The experimental protocol is as follows: Ions are first cooled to near the motional ground state using sideband cooling. After ground-state cooling, we determine the initial mean mode occupation to be approximately 0.7 phonons for both the common and stretch modes of the double-well system. After ground-state cooling, a  $397 \text{ nm}$  pulse is applied to ions in only one of the wells (which we will call the first well), exciting them to the  $4P_{1/2}$  level. Spontaneous decay to the  $4S_{1/2}$  level induces random momentum kicks, exciting the motion of those ions. Spontaneous decay can also occur to the meta-stable  $3D_{3/2}$  state with a branching ratio of about  $1/16$ , where population is trapped, and the ion has left the heating cycle. A duration of  $5 \mu\text{s}$  of the  $397 \text{ nm}$  pulse ensures that  $> 99.9\%$  of population has been shelved to the  $3D_{3/2}$  level, from where it is hidden from subsequent operations.

At this stage, ions in the first well have endured some motional heating, while those in the second remain near the motional ground state, corresponding to the initial condition of Eq. 15. We probe the motional excitation of the second well by analyzing optical excitation from two types of analysis pulses, either red or blue detuned from a  $4S_{1/2}$  to  $3D_{5/2}$  carrier transition by the mean motional frequency. The mean phonon number in the second well is inferred by comparing the excitation of both sidebands to numerical models of excitation as a function of energy stored in the well. Since the ions in the left well are hidden from these analysis pulses, they do not need to be

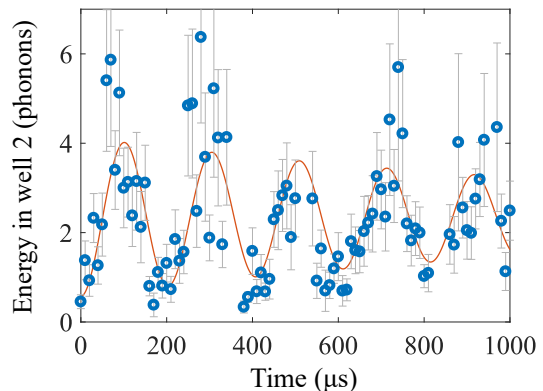


FIG. 5. Demonstration of exchange of motional excitation between two axially coupled sets of two ions. After ions in one well are excited, the excitation of ions in the second well is measured as a function of delay time between excitation and measurement. The solid line is sinusoidal fit, with a decay parameter included. A coupling rate of  $\Omega_c = 2\pi \ 4.7(1) \text{ kHz}$  is inferred from the rate of excitation transfer.

considered in the numerical models. The sideband excitation pulse is on for a duration of  $15 \mu\text{s}$ . The total duration of motional excitation and analysis,  $20 \mu\text{s}$ , is shorter than the expected energy exchange time,  $t_{\text{exc}} \approx 100 \mu\text{s}$ , but is not negligible. Since excitation transfer also occurs during these pulses, we expect a reduction in contrast in the amplitude of the phonon exchange measurement.

Fig. 5 displays the measured energy of the ions in the second well,  $E_2$ , expressed in terms of phonons,  $E_2/\hbar\omega_z$ , as a function of wait time between excitation of the first well, and analysis of the second. The expected oscillatory exchange of energy is apparent. The red line is a least-squares fit between the measured data and the model

$$\frac{1}{2} ((n_1 - n_2) \cos(\Omega_c t + \phi) \exp(-t/\tau_d) + n_1 + n_2) \quad (16)$$

with  $t$  the experimental wait time and all other variables free fitting parameters.  $n_1$  and  $n_2$  represent the first and second well's initial local phonon number,  $\Omega_c$  is the coupling rate,  $\phi$  is a phase offset caused by non-zero duration of the state preparation and analysis pulses, and  $\tau_d$  represents a decay in contrast due to motional decoherence. From the fit we determine a coupling rate of  $\Omega_c = 2\pi \ 4.7(1) \text{ kHz}$ , in good agreement with the coupling rate measured through spectroscopy (as in the previous section) and with the numerically predicted value,  $2\pi \ 4.9 \text{ kHz}$ .

### C. Heating rates

Coherent quantum information with continuously larger ion-strings relies on motional coupling between its constituent ions. These procedures require the motional states of the chain of ions to be coherent, since the motional modes act as a data bus. An increase in mode



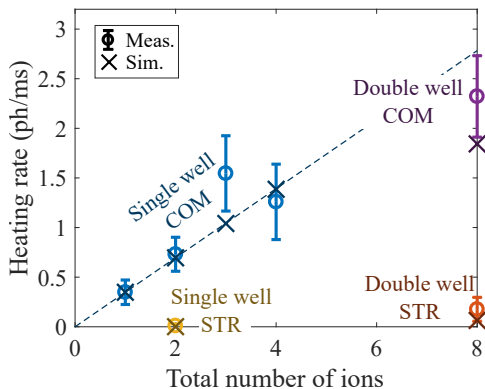


FIG. 6. Heating rates for various configurations of ions, in a single well or double well. Circles are measured data. Crosses are simulated values, using the single ion data as a calibration reference. The dashed line represents a linear scaling of heating rate with number of ions, following a point charge model, also using the single ion data as a reference.

occupation over time, a mode’s heating rate, is a common issue in surface traps [22–26]. In this section, we investigate the properties of mode heating of ion crystals confined in a double-well potential.

Fig. 6 displays the results of heating rate measurements for various ion numbers measured via excitation of the motional sidebands [22]. In all measurements the frequency of the measured mode is set to 450 kHz. For the double-well data, the wells are separated by 50  $\mu\text{m}$ . The blue circles are a set of control measurements in which ions are trapped in a single well. These measurements have been performed to confirm the expected linear scaling of the heating rate with number of ions [22]. The single particle data is furthermore employed to calibrate a technical noise model of electrode voltage noise, which is used to determine a simulated expected heating rate for the other measured configurations. Simulated data are marked as crosses in Fig. 6. The noise model is described in Section II C, assuming technical voltage noise that is uncorrelated between different electrodes but each electrode is on a constant potential.

Double-well heating rates have been taken with four ions per well. The heating rate of the common mode of motion, 2.4(4) ph/ms (purple circle in Fig. 6), is similar to that which would be expected from an 8-ion point charge model, 2.7 ph/ms (dashed line). However, the measured heating rate lies lower than this value, due to the spatial distribution of charges. The predicted heating rate when taking the spatial extent of the ion chain into account is 1.8 ph/ms (purple cross). The stretch mode, in contrast, has roughly an order of magnitude lower heating rate, 0.2(1) ph/ms (red circle), in agreement with the predicted value of 0.1 ph/ms (red cross).

The fact that the stretch mode of motion exhibits a lower heating rate than the common mode is well-known for single-well ion crystals (exemplified by the yellow data point in Fig. 6). We have demonstrated here for the first

time that this concept continues to hold even when ion crystals are spatially separated, which highlights the benefit of using the stretch mode for well-to-well entangling operations, compared to merging and splitting protocols, which are inherently sensitive to mode heating.

The double-well stretch mode has the property that its motional frequency remains as low as the common mode frequency. A lower motional frequency is generally considered favorable, since the duration of an entangling gate is shorter at low motional frequencies. In contrast, in single-well ion crystals the stretch mode has a factor  $\sqrt{3}$  higher frequency. This, in combination with the fact that in a multi-ion stretch mode ions unequally contribute to the mode (i.e., have unequal Lamb-Dicke parameters), makes the use of the stretch mode and higher order modes for entangling operations less common. The double-well stretch mode does not suffer from these disadvantages even for large numbers of ions per well,  $n$ , and is a good candidate for mediating entangling operations due to its low heating rate.

#### IV. WELL-TO-WELL COUPLING IN THE RADIAL DIRECTION

In this section we demonstrate coupling, phonon exchange, and entanglement of radially separated ions in two linear ion traps. Furthermore, we verify that the stretch mode of oscillation of coupled ions in a radial double-well potential is more resilient to electric field noise compared to the common mode.

We realize the following experiments with the trap depicted in Fig. 7(a), which features 3 co-linear RF electrodes and a total of 12 DC electrodes distributed on a single aluminum metal layer on top of a fused silica substrate. As discussed in Section II, ion strings are stored at the minimum of the effective trapping potential generated by the RF electric field, which is commonly referred to as the RF pseudopotential. For the trap in Fig. 7(a), similar to those documented in Refs. [11, 28, 29], the presence of three RF electrodes in a plane results in a pseudopotential landscape that is characterized by having two minima, as shown in Fig. 7(b). For our particular trap, we have determined the well-to-well separation to be  $d \approx 29 \mu\text{m}$  along the radial direction  $x$ , at a height above the surface of 80  $\mu\text{m}$ . A predetermined set of voltages on the DC electrodes allow us to generate individually controllable confining potentials along the axial direction of each of the linear traps, shown in Fig. 7(c) for the right trapping site.

##### A. Coupling rate

The coupling of axial modes of oscillation of ions located in a radially separated double-well potential is demonstrated by measuring the axial mode frequencies of a system of one ion in each well as function of the well-

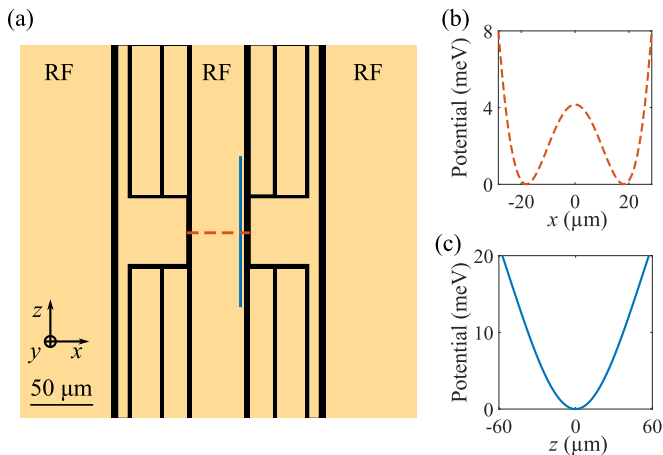


FIG. 7. Trap overview for radial coupling. a) Schematic trap design. The unlabelled electrodes are the DC electrodes used for confinement and control of the two trapping sites. Two additional DC electrodes, not shown in the image, are present alongside the outer RF electrodes. b) Cross section of the total potential along the radial direction  $x$  corresponding to the orange dashed line in (a), generated by applying an RF voltage of 140 V peak-to-peak at 19 MHz on the RF electrodes. The resulting radial frequency along  $x$  is 2.4 MHz in both trapping sites. (c) Cross section of the total potential along the axial direction  $z$  (blue line in (a)), with an axial frequency of 1 MHz.

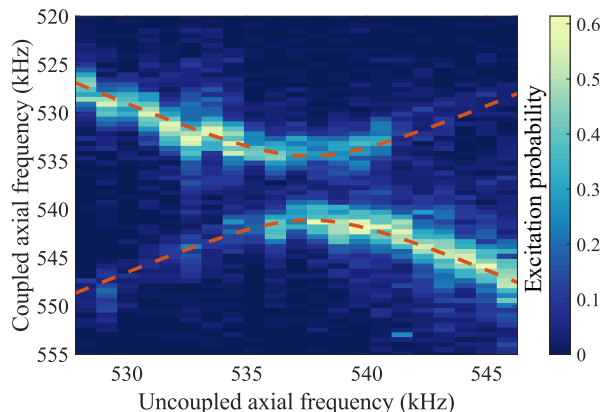


FIG. 8. Avoided crossing measurement for  $n = 1$  ion per well at an axial frequency of 540 kHz. The measurement shows spectra of the ion on the left well as function of the expected left well frequency from the potential curvature, in the absence of well-to-well coupling.

to-well axial frequency detuning. As discussed in Section III A, upon tuning the two wells on resonance, the axial mode spectrum exhibits an avoided crossing, and the minimum frequency difference represents the coupling rate  $\Omega_c$  when the two wells are resonant. We change the axial frequency in the two wells using two sets of DC electrode voltages, each of which controls the potential curvature in one of the two potential wells, without affecting that of the other. Subsequently, we scan the axial curvature of both wells in opposite directions, and

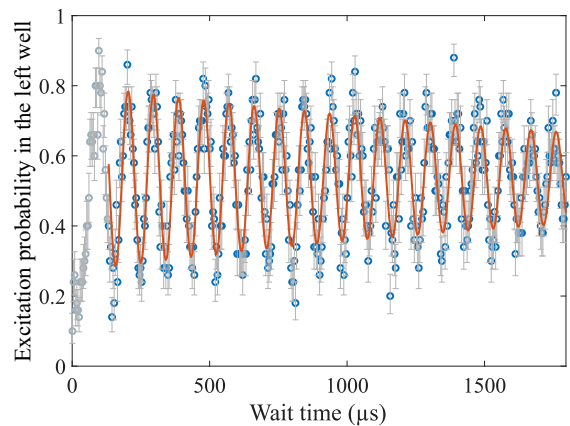


FIG. 9. Demonstration of phonon exchange between axial modes of oscillation of two radially coupled wells with  $n = 1$  ion in each. The solid line is a sinusoidal fit, with a decay parameter included. The greyed out data before 130  $\mu\text{s}$  is not included in the fit as the motional frequencies of the two wells have not settled after switching DC voltages. From the rate of phonon transfer we infer a coupling rate  $\Omega_c = 2\pi 10.92(2)$  kHz.

deduce the axial modes' frequency via sideband spectroscopy with a 729 nm laser beam which is aligned to both wells simultaneously. We read out the electronic state of the ion in the left well by collecting its fluorescence light with a photomultiplier tube (PMT). By filtering out the light from the right well with an aperture, we observe the axial mode of only the ion on the left well, which splits into two as it approaches resonance with the right well.

The measured spectra of the ion in the left well are shown in Fig. 8, as a function of the expected left well axial frequency extracted from the potential curvature, in the absence of well-to-well coupling. We obtain the motional frequencies for each axial curvature by fitting experimental data with a double Gaussian function. As explained in Sec. III A, we then compare the extracted mode frequencies to Eq. 12 and obtain  $\Omega_c$ . For  $n = 1$  ion in each well trapped at an axial frequency of 540 kHz, we extract a coupling rate  $\Omega_c = 2\pi 6.6(3)$  kHz. This value is in good agreement with that expected from Eq. 4,  $2\pi 7.0$  kHz.

## B. Phonon exchange

As introduced in Sec. III B, coherent exchange of motional excitation from one well to another is a prerequisite to perform well-to-well entangling operations. In this section we present phonon exchange between two ions located in two radially separated linear traps.

The experiment consists of injecting one phonon in one of the two wells, and the observation of phonon transferring from one well to the other as a function of the wait time after the phonon injection. In contrast to the axial phonon exchange presented in Section III B, we do, in

our current setup, not have the means to individually address ions with our laser beams. Instead, we realize selective phonon injection by implementing fast in-sequence voltage switching on the trap's DC electrodes, allowing us to tune the motional frequencies of the two wells in and out of resonance. The two wells become spectrally resolved when out of resonance, allowing us to perform ion-selective operations through sideband pulses.

To perform the experiment, we cool the ions to near the motional ground state via sideband cooling. Subsequently, we tune the two wells out of resonance, and inject one phonon in a target well with a blue sideband  $\pi$ -pulse. We then tune the two wells on resonance, enabling phonon exchange between the two ions. After a given wait time, we detune the wells from resonance again, and use a blue sideband  $\pi$ -pulse on the target ion. If a phonon is present in the target well, this pulse reverses the excitation of the first pulse, de-exciting the ion. If, on the other hand, the phonon was transferred to the other well, no de-excitation occurs. The ion's motional state is correlated with its electronic state, and can thus be detected directly through fluorescence detection.

The result of the phonon exchange measurement for a system of  $n = 1$  ion per well, at an axial frequency of 540 kHz is shown in Fig. 9. Switching the wells into resonance does not happen instantaneously, as the adjusted voltages pass through electronic filters. Therefore, there is a non-zero time during which the two wells are near, but not on, resonance. We have independently determined that the motional frequencies settle to a steady state at approximately  $130 \mu\text{s}$ , after which phonon exchange is expected to occur at a constant rate. Wait times prior to this are indicated by the faded region before  $130 \mu\text{s}$  in Fig. 9.

The red line represents a least-squares fit between the measured data and a model equivalent to the one used in Sec. III B, Eq. 16. Data from the first  $130 \mu\text{s}$  are not included in the fit. We infer a coupling rate  $\Omega_c = 2\pi 10.92(2)$  kHz. This value differs from the value obtained from the avoided crossing measurement in the previous section,  $2\pi 6.6(3)$  kHz. This discrepancy comes from the fact that the frequencies of the two wells were intentionally set to be marginally off-resonance. This detuning from resonance was introduced to counter a loss in phonon exchange contrast caused by the non-zero switching time, in which partial phonon exchange occurs before resonance is reached. This effect is discussed in more detail in Appendix A.

### C. Heating rates

As has been introduced in theory in Section II C, the modes of a set of coupled ions in a double-well potential are unequally affected by electric field noise. In particular, for typical trapping geometries, the stretch mode of motion is considerably less sensitive to electric field noise compared to the common mode. This has been experi-

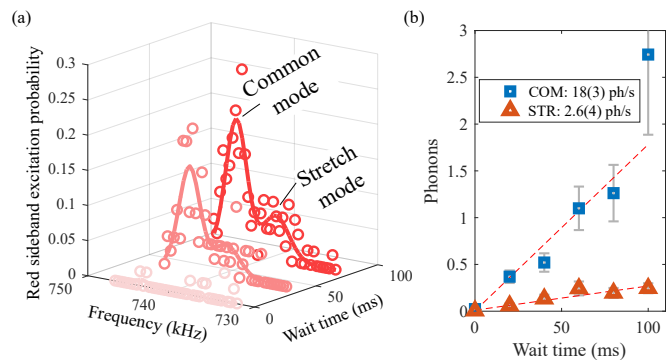


FIG. 10. Results of heating rate measurements for radially separated ions. (a) Spectra around the red sideband transition depict the emergence of peaks as wait time between state preparation and sideband analysis increases. Notably, the stretch mode heats up less than the common mode. (b) Phonon numbers are extracted from spectra such as in (a) for various wait times. Heating rates of  $18(3)$  and  $2.6(4)$  ph/s are obtained from linear fits.

mentally shown for ions coupled along the axial direction in Section III C. In this section, we discuss measurements of heating rates of modes emerging from ions coupled in the radial direction.

The heating rate measurements are taken for one ion per well, with an axial motional frequency of 740 kHz. Fig. 10(a) shows examples of excitation spectra of the red sideband for various wait times. Spectra are obtained by detecting the state of only one of two ions, while the sideband pulse is applied to both. The emergence of peaks in the red sideband spectrum with an increase in wait time are indicative of an increase of phonon number. Notably, the common mode of motion increases at a higher rate than the stretch mode. By comparing data to numerical models, we obtain phonon numbers as a function of wait time, shown in Fig. 10(b). From linear fits of the data, we obtain heating rates of  $18(3)$  ph/s and  $2.6(4)$  ph/s for the common and stretch modes, respectively.

Simulations that assume uncorrelated voltage noise on the trap electrodes, as discussed in Section II C, predict that for ions separated by  $29 \mu\text{m}$ , the ratio of common and stretch mode heating rates is 16. Our measured ratio, 8.4, deviates from this prediction, which indicates that ion heating rates in our trap are not limited by the technical voltage noise described in our noise model. Regardless, the stretch mode heating rate is still lower than that of the common mode of motion of a single-well two-ion system, which we have measured to be 7 ph/s.

### D. Entanglement

The generation of entanglement across quantum registers is an essential tool for the proposed 2D trap array architecture. In this section, we present the realization of entanglement of two radially coupled ions, located in

two distinct linear traps. We encode the entangled quantum information in the internal electronic states of the  $^{40}\text{Ca}^+$  ions,  $4S_{1/2}(m = -1/2)$  and  $3D_{5/2}(m = -1/2)$ , from here using the shorthand notation  $S$  and  $D$ . We use the basis  $|A_1 A_2, n_1 n_2\rangle$  to describe the two-ion system, where  $A_k \in \{S_k, D_k\}$  represents the electronic states, and  $n_k$  the phonon occupation, of ion  $k = 1, 2$ . In the entanglement generation sequence, we consider the two wells on resonance in default operation, while we detune them out of resonance to enable individual ion addressing by applying either red or blue sideband pulses resonant with a target well.

The experimental sequence, schematically shown in Fig. 11(a), is described in Tab. I, where bsb and rsb denote respectively that a blue or a red sideband pulse is applied to ion  $k = 1, 2$ .

TABLE I. Sequence for entanglement generation through well-to-well coupling. Bsb and rsb are pulses applied to blue and red sidebands, respectively.

Step	Operation	State
1	Initialize	$ S_1 S_2, 0_1 0_2\rangle$
2	$\pi$ -pulse bsb, ion 1	$ D_1 S_2, 1_1 0_2\rangle$
3	Coupling on	
4	wait $t \approx \pi/(2\Omega_c)$	$\frac{1}{\sqrt{2}}( D_1 S_2, 1_1 0_2\rangle +  D_1 S_2, 0_1 1_2\rangle)$
5	Coupling off	
6	$\pi$ -pulse bsb, ion 1 rsb, ion 2	$\frac{1}{\sqrt{2}}( S_1 S_2, 0_1 0_2\rangle +  D_1 D_2, 0_1 0_2\rangle)$

After the entanglement sequence, we apply a carrier  $\pi/2$ -pulse, allowing us to alter the parity of the Bell state. The contrast in parity as a function of phase of this analysis pulse corresponds to the coherence of the entangled state.

In Fig. 11(b) we show the state evolution of both ions under the entanglement operation, as a function of the time the ions are kept on resonance. Similar to the phonon exchange measurement described in Section IV B, further explained in Appendix A, the two wells' motional frequencies require time to settle to a steady state after switching the trap's DC potentials. This settle time is indicated in Fig. 11(b) with the faded region at wait times below 130  $\mu\text{s}$ . For higher wait times, an oscillatory behavior between the  $|S_1 S_2\rangle$  and  $|D_1 D_2\rangle$  states is observed. Notably, we observe the entangled state  $1/\sqrt{2}(|D_1 D_2\rangle + |S_1 S_2\rangle)$  at a wait time of 180  $\mu\text{s}$ . In Fig. 11(c) we show the mean populations of the two ions, calculated from 800 repetitions of the sequence at this wait time, from which we extract a mean population of  $P = P_{\text{SS}} + P_{\text{DD}} = 0.86(2)$ .

In Fig. 11(d) we show the parity of the final state as function of the phase of the analysis pulse. The parity contrast corresponds to a visibility of 0.65(2), from which we calculate an entangled state fidelity of  $F_{\text{Tot}} = 0.76(2)$  [30].

## V. ION TRANSPORT IN THE RADIAL DIRECTION

### A. Concept and experimental implementation

Radial transport of ion strings is important as altering the distance between linear ion traps enables connectivity across the linear traps along the 2D ion trap array. In this section we demonstrate control over the radial distance between two parallel linear traps by varying the RF confinement, and validate the theoretical model presented in Section II for radial coupling of axial modes of two ion chains as a function of chain separation and number of ions per well.

We realize these experiments with a trap similar to the one introduced in Section IV, but where the inner and outer RF electrodes have dimensions of 75  $\mu\text{m}$  and 255  $\mu\text{m}$  and are separated by 115  $\mu\text{m}$ . A more detailed description of the trap can be found in Appendix B.

As mentioned in Section IV, the presence of three RF electrodes in a plane results in a potential landscape, which is characterized by having two minima. The aim of this experiment is to control the distance between these RF minima, which depends on the ratio between the voltage amplitudes of the signals applied to the inner and outer RF electrodes,  $\zeta = V_{\text{RF1}}/V_{\text{RF2}}$ . Moreover, the positions of the RF pseudopotential minima depend on the relative phase between the RF signals, which should be set to zero to avoid inducing excess micromotion [31].

Radial shuttling of ions is thus achieved by independently controlling both the amplitude and phase of the RF voltage applied to the inner and outer RF electrodes, using two RF sources and resonators. Phase control of both RF fields is necessary during RF transport, as the relative phase between the RF signals on the trap electrodes is expected to change when varying the RF ratio  $\zeta$ , both due to the coupling between the two resonators, and due to an overall change in the RF circuitry parameters induced by temperature changes. The details about the double resonator circuitry are provided in Appendix B. During RF transport, while the RF ratio is changed, the DC voltages used to confine the ions axially have to be adjusted to keep the DC and RF potential minima overlapped.

### B. Characterization of radial shuttling

We verify our control over the double-well pseudopotential by measuring how the well-to-well distance and radial trap frequencies depend on the RF ratio  $\zeta$ . We keep the axial motional frequency constant at  $\omega_z = 2\pi 540$  kHz for all experimental settings.

The distance between ions is determined by analyzing EMCCD images. For obtaining this distance, the magnification of the camera must be known. This is calibrated as follows: two ions are placed in a single well, and their axial trap frequency is measured using conventional

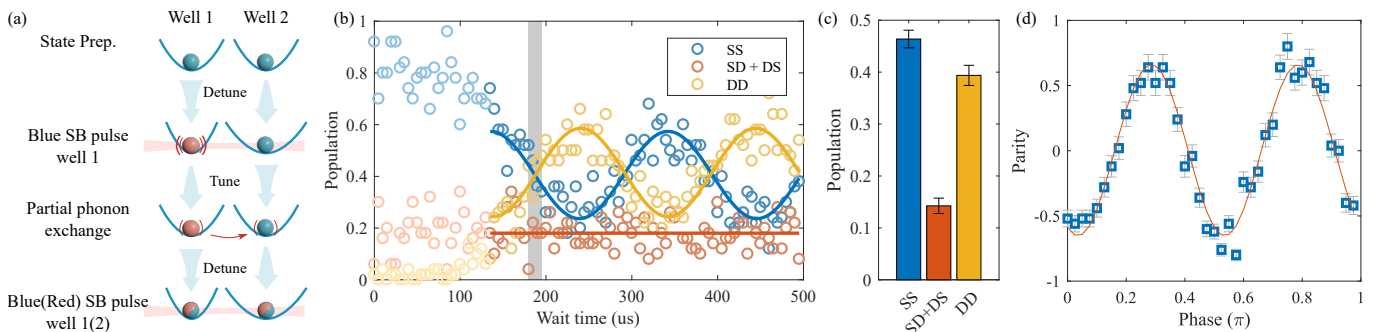


FIG. 11. Entanglement of radially separated ions. (a) Measurement scheme, which relies on tuning the motional frequencies of the two wells out of resonance to allow ion-selective phonon injection and removal with red and blue sideband (SB) pulses. (b) Measured two-ion populations, as a function of duration that ions are kept in resonance, and phonon exchange can take place. (c) Mean populations, taken at a wait time of  $180\ \mu\text{s}$ , corresponding to the shaded area of (b). A mean population of  $P = P_{\text{SS}} + P_{\text{DD}} = 0.86(2)$  is measured. Averages and their uncertainties, shown by the error bars, are taken from 800 repetitions of the experimental sequence. (d) The contrast in parity analysis indicates a visibility of  $0.65(2)$ .

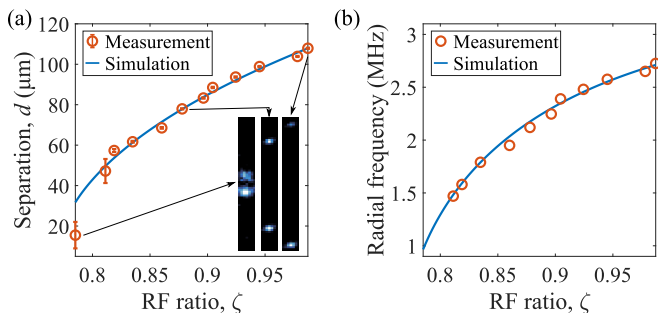


FIG. 12. Characterization of radial transport. (a) Measurement of the well-to-well separation along the  $x$  axis and comparison with simulations. The insets are camera images of ions at the corresponding values of RF ratio  $\zeta$ . (b) Measurement and simulations of the radial frequency parallel to the trap surface, as function of  $\zeta$ , for a constant axial frequency of  $\omega_z = 2\pi\ 540\ \text{kHz}$ . The error bars are smaller than the markers, as the measurements' uncertainty is of the order of  $1\ \text{kHz}$ , and are thus not shown in the plot.

sideband spectroscopy. The separations of ions in pixels are compared to the analytically expected separation for given trap frequencies [32].

In Fig. 12(a) we show how the well-to-well distance depends on  $\zeta$  by setting the two wells to separations between  $d = 15\ \mu\text{m}$  and  $110\ \mu\text{m}$ . The separation  $d \approx 15\ \mu\text{m}$  is the limit below which the two wells merge into a single one. Well-to-well separations above  $110\ \mu\text{m}$  is feasible, but in our set-up the cooling lasers are not broad enough to address both wells simultaneously at a larger separation. The results presented are in good agreement with the pseudopotential simulations up to a constant scaling factor of  $1.039(5)$ , which rescales the measured RF ratio. This factor comes from systematic errors in the measurement of the RF voltage on the trap.

In Fig. 12(b) we show the frequency dependence of the  $x$  radial mode of oscillation as a function of  $\zeta$ . We

determine this frequency by applying an RF signal that is resonant with the ions' motional frequency to one of the trap DC electrodes. This process, colloquially known as RF tickling [33], excites the motion of a trapped ion to an extent that it becomes visible on a EMCCD camera. The “tickling” method is used as opposed to the previously mentioned sideband spectroscopy, because it reduces ambiguity in determining radial modes.

In varying  $\zeta$ , only the inner RF voltage is changed, while the outer RF electrodes are kept at a constant voltage. The RF ratios of the data in Fig. 12(b) include the scaling factor determined from the data in (a). From numerical simulations, we expect the radial frequencies to decrease as the RF voltage ratio approaches 0.8, where the two radial wells merge into a single one. We show that the measured radial frequencies decrease according to simulations. The presented measurements indicate that we understand and can control the RF double-well pseudopotential, allowing us to tune the radial distance between the two wells, and thus control the coupling rate of ion chains.

### C. Coupling rate

The coupling rate between ion chains in separate wells is determined experimentally by detecting the motional mode frequency of the ions in the two wells. As described in Section II, the mode spectrum of two coupled oscillators splits into an in-phase (common) and out-of-phase (stretch) mode of oscillation. When the wells are tuned on resonance, the frequency difference of these modes is given by the coupling rate  $\Omega_c$ .

Ideally, we would determine the wells' motional mode frequencies via resolved  $729\ \text{nm}$  laser spectroscopy, as described in Section III A. However, in this dual-resonator driven trap, the ion heating rates are on the order of tens of phonons per millisecond, which broadens the coupling

to motional modes and complicates the overall mode spectra. This makes an accurate determination of coupling rates on the order of kilohertz using laser spectroscopy impractical.

Instead, we determine mode frequencies via the RF-tickling method described above. We select the DC electrodes such that the field from the applied RF signal has an overlap with both the in-phase and out-of-phase axial modes of oscillation of ions in the radial double-well. When the RF signal is on resonance with an axial mode, it increases its energy, and we can detect the driven motion by measuring the width of the ion crystals on a CCD camera. When the two wells are on resonance, a scan of the RF tickling frequency excites the coupled system's common and stretch modes at different frequencies, where the frequency difference indicates the coupling rate. If the wells are properly tuned on resonance, the ions in both wells are expected to participate equally in the excitation of both modes. We perform such measurement for the  $n = 3$  ions per well system shown in Fig. 13(a). The width of the ion's image, as detected on the EMCCD camera, is displayed as a function of the RF tickling frequency in Fig. 13(b). Both modes of oscillation are present simultaneously in the two wells, indicating that they are coupled. The unequal excitation of the two modes, seen as differing widths of the peaks in Fig. 13(b), is due to the unequal spatial overlap between the applied RF tickling field and the mode vector. The frequency separation between the modes gives the coupling rate, estimated to be  $\Omega_c = 2\pi \cdot 6.4(3)$  kHz.

Following the above-mentioned approach, we collect the measured coupling rates for double-well configurations of up to  $n = 3$  ions per well, for different well-to-well distances and axial frequencies varying between 238 kHz and 312 kHz. The results are shown in Fig. 13(c), and are compared to simulated values, computed with the approach described in Section II. We measure coupling rates as high as  $\Omega_c = 2\pi \cdot 15$  kHz for one ion per well at a well-to-well distance of 29  $\mu\text{m}$ , and coupling rates between  $2\pi \cdot 5$  kHz and  $2\pi \cdot 10$  kHz for configurations of two or more ions per well. The measured coupling rates agree within 10% with the simulated values.

Despite the good agreement with theory, the coupling measurement described in the previous paragraph does not unambiguously prove that the two wells are coupled, as we did not perform a full avoided crossing scan that indicates the emergence of the coupled modes. To confirm that the radially separated ions are coupled, we measure the relative phase of the ion motion in the two wells for both the inter-well common and stretch mode. More specifically, we perform photon correlation measurements using a PMT and a time tagger, using the RF tickling signal as a trigger. The velocity of the ions in the two wells is modulated at the frequency of the RF tickling signal. Therefore, the ions' Doppler-shift dependent fluorescence rate is likewise modulated. Thus, when correlating PMT photon detection counts with the RF tickling signal, this modulation appears as a sinusoidal signal. These signals

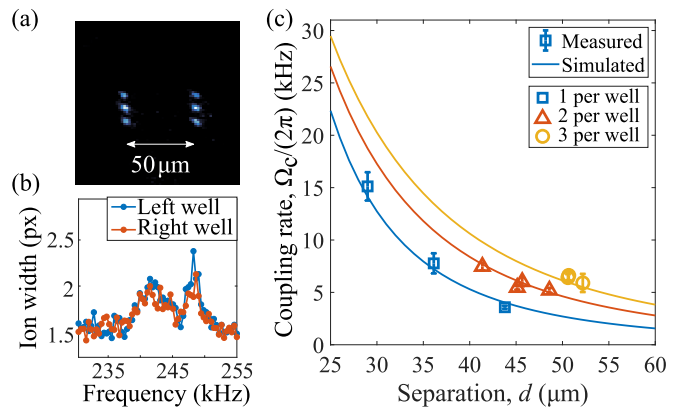


FIG. 13. RF coupling measurement with RF tickling. a) EMCCD image of ions trapped in a radial double well, with three ions per well. b) Width of the ion's image on the EMCCD camera, as a function of the RF tickling frequency. The participation of the ion motion to the two coupled modes in both wells is detected. (c) Well-to-well coupling  $\Omega_c$  as function of distance  $d$  between wells, and number of ions per well. The measurements are taken for axial frequencies ranging from 238 to 312 kHz. The lines in the plot represent radial coupling simulations for different ion numbers at a fixed axial frequency of 262.2 kHz, i.e. the mean of the axial frequencies used in the measurements.

are obtained for the two wells separately by means of an adjustable aperture which is aligned to one of the two wells at a time. In our measurements, we determine both the amplitude and phase of the correlation signals. In the case of the common mode of motion, the detected phases are expected to be equal, whereas for excitation of the stretch mode, the signals are out of phase.

In the photon correlation measurements, we trap one ion per well, separated by 33  $\mu\text{m}$ , and set the axial frequency to be  $\omega_z \approx 2\pi \cdot 225$  kHz. The result of these measurements are shown in Fig. 14, which displays the mean amplitude of the correlation signals of the two wells as a function of the frequency of the RF tickle voltage. The colors of the data points indicate the relative phase between the signals of the two wells. As expected, we observe one mode of oscillation where the ions oscillate in phase with each other, and another where they oscillate out of phase. The measured mode splitting agrees with the simulated value of  $2\pi \cdot 10$  kHz.

## VI. 2D-ARCHITECTURES FOR QEC CODES

A two-dimensional lattice architecture, as presented in this work, inherently supports quantum error correcting (QEC) code structures and provides an ideally suited platform for scalable fault-tolerant (FT) QEC. Specifically, the combination of axial and radial shuttling supports all-to-all connectivity between ions in separate strings. This is essential for scalable quantum computing, which requires the ability to detect if a qubit has transi-

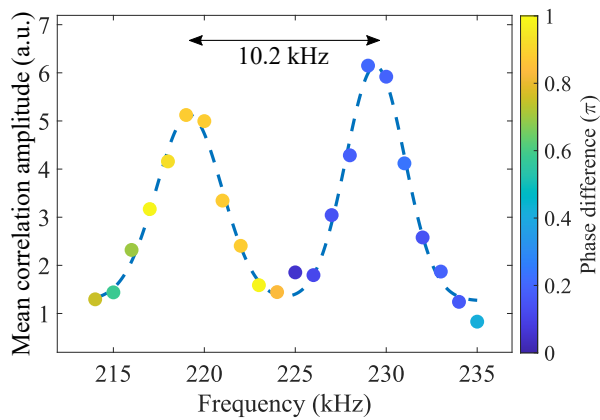


FIG. 14. Phase difference of the photon correlation signals of each well, as a function of the RF tickling frequency. The plot shows the mean of the correlation amplitude of the correlation signals collected in the two wells, and the dashed line is a guide-to-the-eye double-Gaussian fit. For the stretch mode, the ion in one well oscillates out of phase with respect to the one in the other well. For the common mode, the ions in the two wells oscillate in phase.

tioned into an unwanted state and to correct these errors in a sufficiently reliable way [34, 35]. One approach to increase the accuracy of quantum algorithms is to encode quantum information across multiple physical qubits: errors on physical qubits can be corrected by performing QEC and, thereby, the information encoded in a logical state can be recovered [36, 37].

To illustrate the potential power of the developed trapped-ion architecture for scalable FT QEC, we outline a few routes which can be naturally hosted and operated in the 2D lattice structure of coupled traps. Fully controllable 2D lattices naturally enable the implementation of topologically-concatenated QEC codes while retaining their inherent code structure. As illustrated in Fig. 1, subsets of ions are confined in separate wells on a 2D lattice, where each potential well can represent a logical qubit of the lower concatenation level. Within each of these wells, two-qubit gates can be carried out between arbitrary pairs of qubits. The different logical qubits are coupled by means of well-to-well entangling gates and form the second layer of concatenation. This architecture directly mimics the code structure of a concatenated surface code. For example, when each physical qubit on a surface code lattice is substituted by an  $[[n_c = 4, k_c = 2, d_c = 2]]$  code, defined by four-qubit stabilizers  $s_X$  and  $s_Z$ , where  $n_c = 4$  physical qubits encode  $k_c = 2$  logical qubits with code distance  $d_c = 2$ , one obtains the  $[[4, 2, 2]]$ -concatenated code [38], as illustrated in Fig. 15(a). By concatenating the surface code and the  $[[4, 2, 2]]$  code, the stabilizer  $S_Z^j$  ( $S_X^i$ ) defined on vertex  $i$  (plaquette  $j$ ) of the surface code lattice (blue, red) is transformed into a weight-8 stabilizer  $S_\sigma^j$  ( $S_\sigma^i$ ) with  $\sigma = Z(X)$  (purple octagon) and the additional stabilizers  $s_\sigma^{(k)}$  (orange square) of the  $[[4, 2, 2]]$  code emerge on each

replaced qubit.

One advantage of concatenating quantum codes is the scaling of the total failure probability: below a certain threshold of the physical error rate, the failure probability is suppressed doubly-exponentially with each layer of concatenation, which enables practical FT quantum computing below this threshold [34, 35]. Furthermore, by concatenating codes with complementary sets of transversal and, therefore FT gates, it is also possible to implement a FT universal gate set [39–41], as for example by using the two-dimensional  $[[7, 1, 3]]$  and the three-dimensional  $[[15, 1, 3]]$  code shown in Fig. 15(b): single errors are prevented from propagating onto multiple qubits on the same encoded block by applying a non-transversal version of the T-gate on the  $[[7, 1, 3]]$  code using only transversal gates of the concatenated  $[[15, 1, 3]]$  code [39]. Access to a FT universal set of gates allows the efficient approximation of arbitrary operations [42] on encoded states and poses a key requisite for error-corrected universal quantum computing. Moreover, concatenated codes have been found to efficiently protect against biased noise [43], which is often present in ion trap quantum processors [44].

Beyond their applications for concatenated codes, two-dimensional architectures open up the possibility to carry out logical operations in a highly parallelized way, which enable the efficient and modular implementation of error correction blocks. By coupling two ion-chains in separate wells, it is possible to, for example, apply CNOT-gates on pairs of qubits as depicted on the left side of Fig. 15(a). This would implement a transversal two-qubit gate on specific codes, which has previously only been realized in a sequential manner [45–48]. Transversal CNOT-gates are a key feature for modular QEC, known as Steane-type error correction [35, 49, 50]. Here, logical auxiliary qubits are coupled to the logical data qubit with a transversal CNOT-gate, which effectively copies errors from the data to the auxiliary qubit, as depicted in Fig. 15(c). By measuring the logical auxiliary qubit, one can directly extract the error syndrome. Compared to other EC schemes, Steane-type error correction requires the lowest possible number of two-qubit gates and can outperform other state-of-the-art EC protocols such as flag-based EC, as has been demonstrated in recent experiments [46, 51, 52]. Readily available logical resource qubits could not only be used for error correction [49, 53] but also as resource states for magic state injection, as for example for the  $[[4, 2, 2]]$  code [54] or the  $[[7, 1, 3]]$  code [55, 56].

Tab. II summarizes the minimal numbers of ions and registers which are required for the proposed QEC protocols. The embedding of these protocols on a fully connected two-dimensional lattice architecture, in principle, enables the implementation of scalable FT QEC and opens up a new route towards FT universal quantum computing on an ion trap quantum processor.

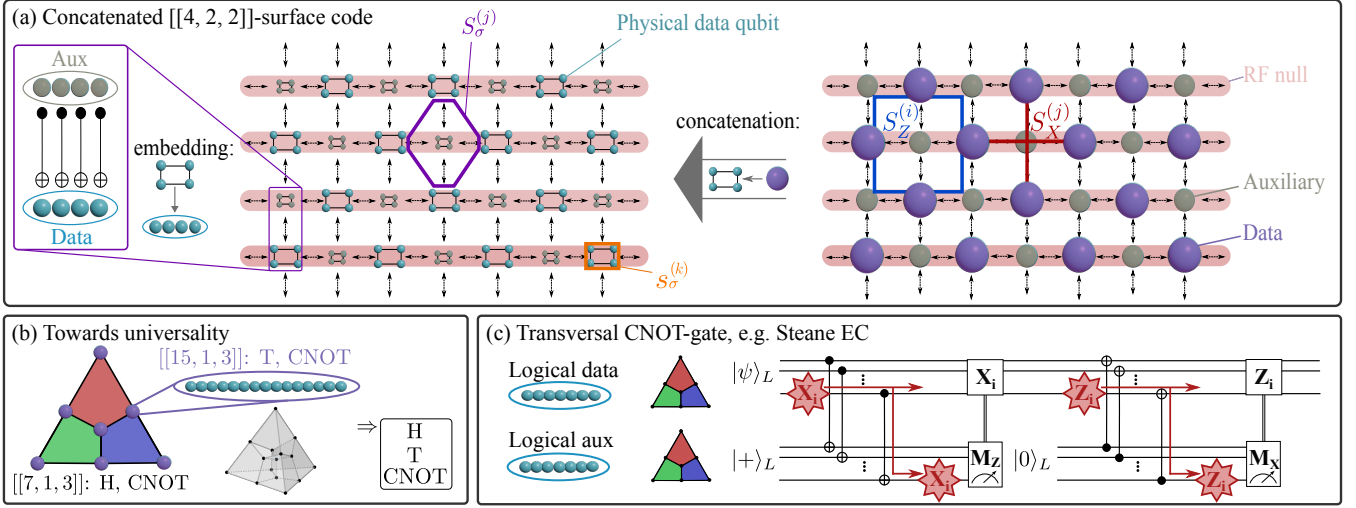


FIG. 15. Applications of the 2D architecture for QEC codes. (a) Concatenated surface code: Every edge in the  $[[n_c = (d_c^2 + (d_c - 1)^2), 1, d_c]]$  surface code (right) is replaced by a square which contains four qubits [38]. In doing so, one can construct a  $[[n'_c = 4(d_c^2 + (d_c - 1)^2), k'_c = 2, d'_c = 2d_c]]$  code on a square-octagon lattice, where each cluster of four qubits resides in one potential well (center). A single auxiliary qubit, depicted in grey (right), in a parity measurement may be replaced by four qubits encoding a logical state of the  $[[4, 2, 2]]$  code [38] (embedding, left). (b) By concatenating the two-dimensional  $[[7, 1, 3]]$  and the three-dimensional  $[[15, 1, 3]]$  color code, one can implement a FT universal gate set  $\{H, T, CNOT\}$  [39–41]. (c) Transversal CNOT-gates enable efficient syndrome readout by means of Steane-type EC [49]. An auxiliary logical qubit is prepared in  $|+\rangle_L$  using the same code as the data qubit and coupled to the data qubit with a transversal CNOT-gate. This copies  $X$ -errors from the data onto the auxiliary qubit. By measuring the auxiliary qubit projectively in the  $Z$ -basis, one can infer the respective syndrome. Analogously,  $Z$ -errors are corrected by preparing an auxiliary  $|0\rangle_L$  and measuring in the  $X$ -basis. These logical auxiliary qubits could be prepared in separate potential wells and readily be used as resource states in the 2D lattice architecture.

TABLE II. Required minimal number of ions per well and number of registers for different QEC protocols: Steane EC on the  $[[7, 1, 3]]$  Steane code [46, 49], which also corresponds to the smallest 2D topological color code [57, 58]; magic state injection (MSI) on the  $[[7, 1, 3]]$  [45, 55, 56]; the implementation of a universal gate set by concatenating the  $[[7, 1, 3]]$  code with the  $[[15, 1, 3]]$  code [41]; and a general distance- $d$   $[[4, 2, 2]]$ -surface code [38]. The given numbers only correspond to the number of required data qubits and registers, and do not take auxiliary qubits into account.

QEC protocol	#Ions per well	#Registers
Steane EC on $[[7, 1, 3]]$	7	2
MSI on $[[7, 1, 3]]$	7	2
Universal gate set	15	7
$[[4, 2, 2]]$ -surface code	4	$d_c^2 + (d_c - 1)^2$

## VII. CONCLUSIONS AND OUTLOOK

In summary, we have proposed and realized the building blocks of a so-called Quantum Spring Array (QSA) architecture, where independent ion-strings are arranged in a two dimensional array, and connectivity is achieved via axial and radial ion transport. We have implemented and characterized coupling between chains of ions in separate wells in both axial and radial directions with respect to the axis along which ion crystals are confined. The coupling rates of our system are compared to the

TABLE III. Summary of well-to-well coupling rates  $\Omega_c$  and interaction constants  $k_{\text{int}}$ .

	Ions per well	Separation $d$ ( $\mu\text{m}$ )	Coupling $\Omega_c/(2\pi)$ (kHz)	Interaction constant $k_{\text{int}}$ ( $\text{keV m}^{-2}$ )	
Ref. [16]	1	40	3.1	26	
	1	54	1.9	16	
	2	54	6	110	
Ref. [15]	3	54	14	370	
	Axial Ref. [17]	1	30	12	177
		2	42	17	230
4		52	25	650	
Ref. [17]	6	56	39	1600	
	Radial	1	29	15	61
		2	41	7.5	61
3		51	6.4	77	

results from references [15–17] in Table III. In references [16, 17] the ion species  ${}^9\text{Be}^+$  is investigated and thus we express the interaction between ions in separate wells in terms of the interaction strength (see  $k_{\text{int}}$  in Eq. 2), which is independent from the frequency and mass. The interaction strength that was observed in our experiments is significantly higher than that of references [15–17].

In the linear surface trap, we have demonstrated axial well-to-well coupling rates of 39 kHz for 6 ions per well.



Moreover, we have shown phonon exchange between axial wells and a reduced heating rate in the double-well stretch mode of oscillation compared to that of the common. The first implementation of radial coupling has been shown in a second surface ion trap. We harnessed this radial coupling to show exchange of a single phonon between axial modes of oscillation of ions located in a radial double well potential. Taking a step further, we have exploited well-to-well single phonon exchange to realize the first demonstration of entanglement of radially coupled ions located in two distinct linear traps.

We demonstrated the capability to control the distance and thus the coupling rate between ions distributed in adjacent linear traps in the array. The radial coupling rates are up to 15 kHz for radial double-wells with up to three ions per well. We expect that ion heating in the double-RF drive configuration used for radial transport will be one of the main challenges for a large-scale implementation. While the observed high heating rate are not fully understood, it is likely caused by phase and/or amplitude fluctuations of the voltages applied to the RF electrodes. We expect that we can overcome this technical obstacle with low-noise electronics and resonators with higher quality factors that decrease bandwidth at which the noise is affecting the motion.

Future research will focus on design and fabrication of surface traps capable of performing both axial and radial shuttling operations within the same trap [11]. Such traps will feature multiple trapping regions in both dimensions. Additionally, the implementation of integrated voltage control electronics and optical elements will allow for localized gate operations between specified lattice sites. We show that the connectivity provided by the QSA architecture readily lends itself to natural embeddings and operation of concatenated quantum error correction schemes.

## VIII. ACKNOWLEDGEMENTS

We gratefully acknowledge support by the European Union’s Horizon Europe research and innovation program under Grant Agreement Number 101114305 (“MILLENION-SGA1” EU Project), the US Army Research Office through Grant Number W911NF-21-1-0007, the European Union’s Horizon Europe research and innovation program under Grant Agreement Number 101046968 (BRISQ), the ECSEL JU (which is supported by European Union’s Horizon 2020 and participating countries) under Grant Agreement Number 876659 (iRel), the Austrian Research Promotion Agency (FFG) under the project “OptoQuant” (37798980), the European support “Important Projects of Common European Interest” (IPCEI) on Microelectronics, the Austrian Science Fund (FWF Grant-DOI 10.55776/F71) (SFB BeyondC), the Austrian Research Promotion Agency under Contracts Number 896213 (ITAQC) and 897481 (HPQC), the Austrian Science Fund (FWF)

[10.55776/COE1] and the European Union – NextGenerationEU, the Office of the Director of National Intelligence (ODNI), Intelligence Advanced Research Projects Activity (IARPA) and the Army Research Office, under the Entangled Logical Qubits program through Cooperative Agreement Number W911NF-23-2-0216. We further receive support from the IQI GmbH. This research is also part of the Munich Quantum Valley (K-8), which is supported by the Bavarian state government with funds from the Hightech Agenda Bayern Plus. M.M. additionally acknowledges support by the Deutsche Forschungsgemeinschaft (DFG, German Research Foundation) under Germany’s Excellence Strategy ‘Cluster of Excellence Matter and Light for Quantum Computing (ML4Q) EXC 2004/1’ 390534769, and the ERC Starting Grant QNets through Grant No. 804247.

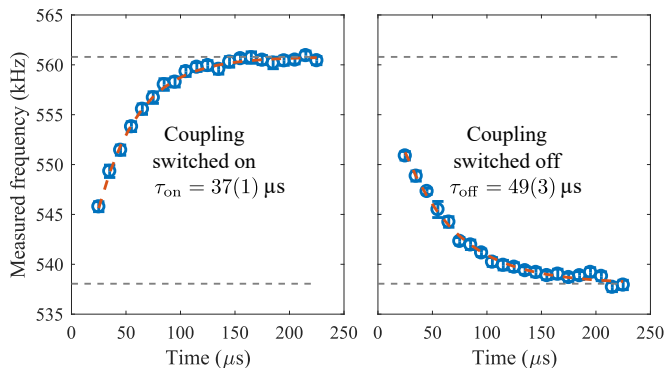


FIG. 16. Characterization of switching time between voltage sets. The plot shows the measured motional frequency of one of the two wells, as a function of wait time after switching wells out of and into resonance. Dashed lines are exponential decay fits, from which we extract characteristic switching times.

### Appendix A: Phonon transfer with DC voltage switching

In Section IV B we have demonstrated an exchange of phonons between radially separated ions and Section IV D has shown that this exchange can be used to generate entanglement between those ions. In both cases, this exchange involves tuning the motional frequencies of the two wells out of resonance to allow addressed sideband pulses to inject a phonon in a chosen well, and into resonance to enable phonon exchange through well-to-well coupling. In both the phonon exchange and entangling measurements the rate of phonon exchange is higher than is predicted from basic theoretical models. This is attributed to having intentionally set the two wells to be near, but not in, resonance for the exchange. The reason for this choice is related to the fact that the switching in and out of resonance does not happen instantaneously, but is gradual due to our built-in electronic filters of DC electrodes to which the voltage changes are applied. The two wells therefore spend some non-negligible time near resonance before settling to a steady state on resonance. While the setting is at near-resonance, partial phonon exchange already takes place, and disrupts the full transfer that would occur at resonance. In this Appendix, we use numerical models to detail this effect and further motivate why we have chosen to do phonon transfer with the two wells not perfectly resonant.

One of the parameters of the calculation is the rate at which motional frequencies of the wells vary over time after DC voltages are switched. We experimentally determine this value by taking spectra around the motional sideband of a trapped ion as a function of wait time after switching DC voltages. The probe time ( $50 \mu\text{s}$ ) is not negligibly small compared to the rate at which motional frequencies change. Since the change in frequency during the probe time is approximately linear, it can be assumed that the measured frequency corresponds to the

motional frequency at half the probe time,  $25 \mu\text{s}$ . The results of this measurement are shown in Fig. 16. The dashed lines are fits using an exponential decay model,  $f = f_{\text{fin}} - (f_{\text{fin}} - f_{\text{init}}) \exp(-t/\tau_{\text{on/off}})$ , with  $f_{\text{init}}$  and  $f_{\text{fin}}$  the initial and final frequencies,  $t$  the time after switching, and  $\tau_{\text{on/off}}$  the characteristic decay time when switching on/off resonance. From the fits we determine  $\tau_{\text{on}} = 37(1) \mu\text{s}$  and  $\tau_{\text{off}} = 49(3) \mu\text{s}$ .

To examine how the non-zero switching time affects the transfer of phonons between wells, we set up a model of coupled harmonic oscillators. The model solves the following differential equation

$$\frac{d^2 \vec{y}}{dt^2} = \begin{pmatrix} -(2\pi f_1(t))^2 + k_{\text{int}} & k_{\text{int}} \\ k_{\text{int}} & -(2\pi f_2(t))^2 + k_{\text{int}} \end{pmatrix} \vec{y} \quad (\text{A1})$$

where  $\vec{y} = (y_1, y_2)$  are the oscillator amplitudes of oscillators 1 and 2,  $f_1(t)$  and  $f_2(t)$  their time dependent oscillation frequencies, and  $k$  the coupling between them. The vector  $\vec{y}$  is initialized as  $(1, 0)$ , representing a phonon occupying the first oscillator (which we will call “well 1”) and no phonons in the second (well 2). Furthermore, we set  $d\vec{y}/dt = (0, 0)$ .

Using experimental parameters of the phonon exchange measurement of Section IV B, we initialize oscillation frequencies to  $f_1(0) = 520 \text{ kHz}$  and  $f_2(0) = 560 \text{ kHz}$ , which represents the frequencies of the two wells in the detuned state. The on-resonance coupling rate is set to  $6.6 \text{ kHz}$ , which corresponds to  $k_{\text{int}} = 141 \text{ keV m}^{-2}$ . At  $t = 0$ , the DC voltages are switched, and the wells exponentially approach resonance with characteristic time  $\tau_{\text{on}} = 37 \mu\text{s}$ , though are set to settle to a detuning that is not necessarily on resonance,  $\Delta f = f_2(t) - f_1(t)$  for  $t \rightarrow \infty$ .

Figure 17(a) shows the results of such numerical calculations, shown as a function of time for several final detunings,  $\Delta f$ . The color plot on the left shows the phonon occupation of the right well as a function of time, where phonon occupation is calculated as the square of the amplitude of motion. The plots on the right show three examples of phonon exchange, taken at final detunings of  $\Delta f = -7.5, 0, \text{ and } 7.5 \text{ kHz}$ . The example at  $-7.5 \text{ kHz}$  results in a transfer frequency of  $\Omega_c = 10 \text{ kHz}$ , similar to what is obtained from the radial phonon exchange measurement, shown in Fig. 9. The data illustrates that bringing the two wells perfectly on resonance does not result in maximal phonon exchange contrast. Instead, it is beneficial to overshoot resonance, and settle on a non-zero detuning of the two wells.

Figure 17(b) shows the contrast in phonon exchange as a function of the final detuning  $\Delta f$ . Also shown is the maximum phonon occupation that well 2 reaches. Results indicate that a maximum contrast in phonon exchange is reached at a detuning between the wells of about  $\Delta f = -7 \text{ kHz}$ . If an optimal transfer of motional information from well 1 to well 2 is desired, the final detuning should be set to about  $-6 \text{ kHz}$ .

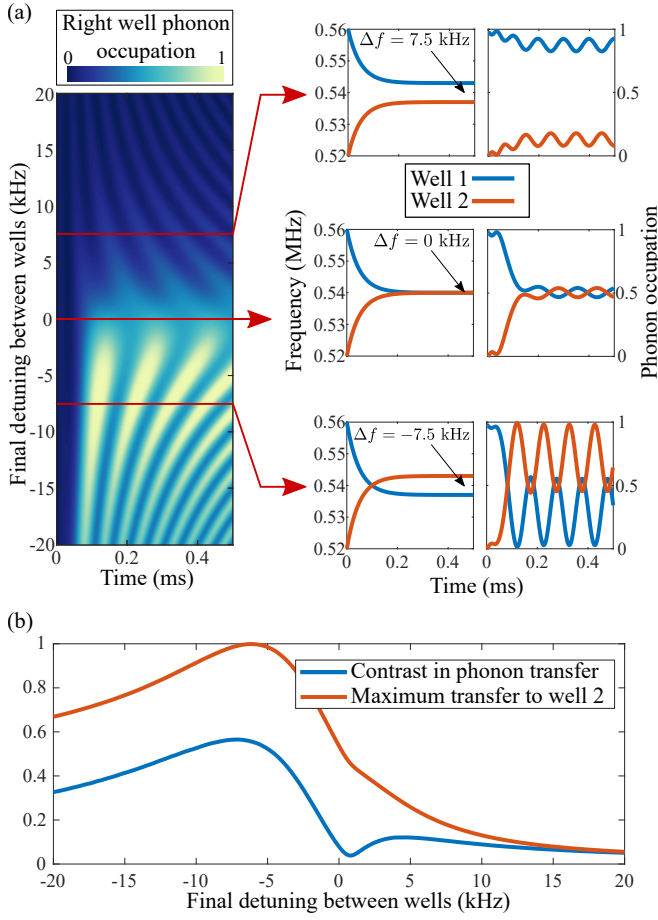


FIG. 17. Results of coupled harmonic oscillator simulations, where two off-resonance oscillators are brought into resonance towards a steady state with a certain “final” detuning. (a) The image on the left displays the phonon occupation in the right well for various final detunings, as a function of wait time. Plots on the right show characteristic examples at  $-7.5$ ,  $0$ , and  $7.5$  kHz. (b) Due to the finite switching speed, the optimal phonon transfer occurs at  $-6$  kHz.

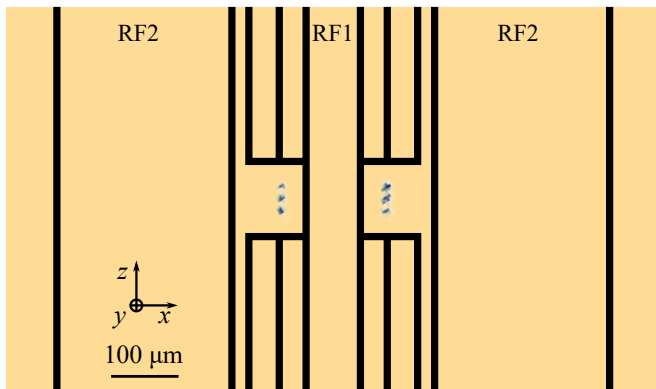


FIG. 18. Schematic of the trap used in the RF transport experiments, with  $n = 3$  ions trapped in each trapping site. Conceptually, the trap design is similar to the one presented in Section IV A. In this case, the inner and outer RF electrodes, RF1 and RF2, have widths of  $75 \mu\text{m}$  and  $255 \mu\text{m}$  and are separated by  $115 \mu\text{m}$ . For RF voltage ratios  $\zeta = V_{\text{RF1}}/V_{\text{RF2}} > 0.8$ , the RF electrode design generates two RF minima separated in the  $x$ -axis,  $\approx 130 \mu\text{m}$  above the trap surface. The unlabelled electrodes are DC electrodes used for generating axial confinement of ions in the two sites.

## Appendix B: Dual RF circuitry

To realize RF shuttling experimentally, we operate the trap shown in Fig. 18 in a cryostat, equipped with two independent RF resonators which are driven by two phase-locked RF sources, similar to the system presented in Ref. [28]. One of the two resonators drives the inner RF electrode, labelled RF1 in Fig. 18, while the other drives the outer RF electrodes, RF2. The diagram and characterization of the RF circuitry that supplies these electrodes is shown in Fig. 19.

An RF voltage signal ( $V_{\text{RF1}}$  for the outer RF electrode, and  $V_{\text{RF2}}$  for the inner RF electrode) is fed into an RF amplifier A, and is then delivered to the RF resonator via a transformer, to decouple the ground of the amplifier from the ground of the cryostat, to which the rest of the circuit is anchored. A variable capacitor  $C_{\text{MA}}$ , and a capacitor  $C_{\text{MB}}$ , placed respectively in series and in parallel to the input signal, are used to match the impedance of the resonator circuit to the  $50 \Omega$  output impedance of the amplifier A. A coil  $L_{\text{S}}$  is used to remove any DC component present in the line. Afterwards, the RF signal reaches the resonator coil  $L_{\text{R}}$ , and the trap electrode  $C_{\text{T}}$ , which together form a resonator circuit. Being close to one another on the trap surface, the inner and outer RF electrodes are capacitively coupled, with coupling capacitance  $C_{\text{C}}$ . The RF signal on the trap is monitored via a capacitive voltage divider placed in parallel to the trap electrode, consisting of the capacitors  $C_{\text{DA}}$  and  $C_{\text{DB}}$ . The resonance frequency of the resonator consisting of the inner RF electrode can be tuned with a variable capacitor  $C_{\text{R}}$ , which is placed. This allows us to match the resonance frequency of the two resonators.

After tuning both the resonance frequency and impedance matching of the two resonators, we measure the transmission, reflection and phase difference of  $V_{\text{RF1}}$  and  $V_{\text{RF2}}$  while the cryostat is at a temperature of  $\approx 10 \text{ K}$ . The measurements are performed using a single RF source connected to the two resonators via an RF splitter, to ensure that a signal with the same phase is fed at the input of both resonators. The reflection of the signal is measured through a bi-directional coupler inserted between the output of the amplifiers and the transformers, while the transmission is monitored via the in-cryo cap dividers.

The results are shown in Fig. 19(b) as a function of signal frequency. Both the transmission and reflection curves indicate that the resonance frequency of the two resonators differs by  $\approx 180 \text{ kHz}$ . However, since the gain curves both have a full-width-half-maximum of  $\approx 300 \text{ kHz}$ , we can drive the resonators at a frequency corresponding to the average of the two resonance frequencies ( $\approx 18.95 \text{ MHz}$ ), while still providing sufficient voltage gain for both.

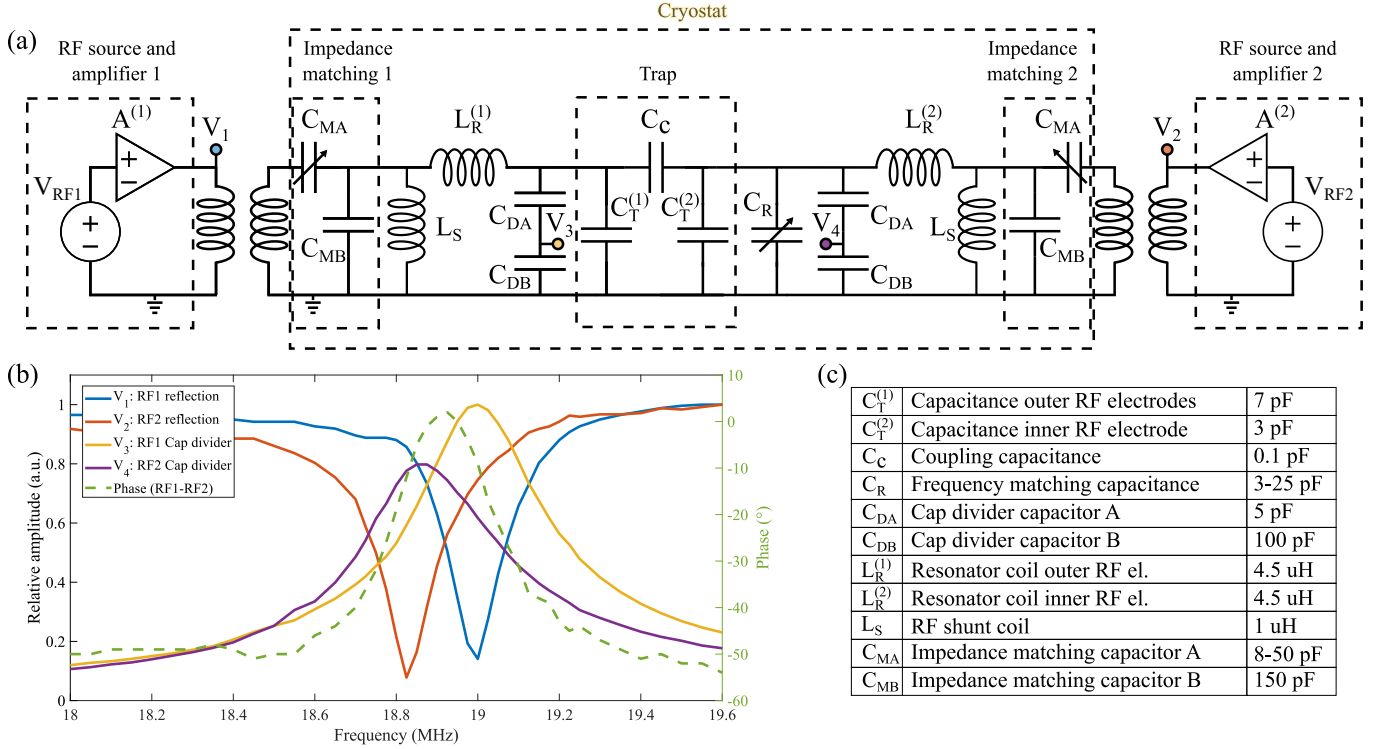


FIG. 19. (a) RF circuitry. Two independent RF sources drive two distinct in-cryo resonators. The resonator circuit 1 drives the outer RF electrode  $C_{T(1)}$ , while resonator 2 drives the inner RF electrode  $C_{T(2)}$ . The two resonators are coupled at the trap via the capacitance  $C_C$ , which couples the inner and outer RF electrodes. A variable capacitor  $C_R$  is soldered in parallel to one of the trap electrodes, allowing us to match the resonance of the two resonators. (b) Resonator characterization. The colored circles in (a) denote the location where the displayed measurements were performed, with respect to ground. The resonators' Q factors differ in the two circuits: The outer RF electrode resonator has a Q factor of 170, and the inner has a Q factor of 120. (c) Table of parameter values for schematic (a). The values of the of the shunt coil  $L_S$  and of the capacitances are taken from the components' data sheets, except for  $C_C$  which is deduced from electrostatic simulations of the trap in Fig. 18. The values of  $L_{1,2}$  are measured with an LCR meter.

- 
- [1] D. Kielpinski, C. Monroe, and D. J. Wineland, *Nature* **417**, 709 (2002).
- [2] J. M. Pino, J. M. Dreiling, C. Figgatt, J. P. Gaebler, S. A. Moses, M. S. Allman, C. H. Baldwin, M. Foss-Feig, D. Hayes, K. Mayer, C. Ryan-Anderson, and B. Neyenhuis, *Nature* **592**, 209 (2021).
- [3] M. Palmero, S. Martínez-Garaot, U. G. Poschinger, A. Ruschhaupt, and J. G. Muga, *New Journal of Physics* **17**, 093031 (2015).
- [4] H. Kaufmann, T. Ruster, C. T. Schmiegelow, F. Schmidt-Kaler, and U. G. Poschinger, *New Journal of Physics* **16**, 73012 (2014).
- [5] M. W. van Mourik, E. A. Martinez, L. Gerster, P. Hrmo, T. Monz, P. Schindler, and R. Blatt, *Physical Review A* **102**, 022611 (2020).
- [6] K. Wright, J. M. Amini, D. L. Faircloth, C. Volin, S. Charles Doret, H. Hayden, C. S. Pai, D. W. Landgren, D. Denison, T. Killian, R. E. Slusher, and A. W. Harter, *New Journal of Physics* **15**, 10.1088/1367-2630/15/3/033004 (2013), arXiv:1210.3655.
- [7] G. Shu, G. Vittorini, A. Buikema, C. S. Nichols, C. Volin, D. Stick, and K. R. Brown, *Phys. Rev. A* **89**, 062308 (2014).
- [8] W. C. Burton, B. Estey, I. M. Hoffman, A. R. Perry, C. Volin, and G. Price, *Phys. Rev. Lett.* **130**, 173202 (2023).
- [9] J. H. Wesenberg, *Phys. Rev. A* **79**, 1 (2009), arXiv:0802.3162.
- [10] S. A. Moses, C. H. Baldwin, M. S. Allman, R. Ancona, L. Ascarrunz, C. Barnes, J. Bartolotta, B. Bjork, P. Blanchard, M. Bohn, J. G. Bohnet, N. C. Brown, N. Q. Burdick, W. C. Burton, S. L. Campbell, J. P. Campora, C. Carron, J. Chambers, J. W. Chan, Y. H. Chen, A. Chernoguzov, E. Chertkov, J. Colina, J. P. Curtis, R. Daniel, M. DeCross, D. Deen, C. Delaney, J. M. Dreiling, C. T. Ertsgaard, J. Esposito, B. Estey, M. Fabrikant, C. Figgatt, C. Foltz, M. Foss-Feig, D. Francois, J. P. Gaebler, T. M. Gatterman, C. N. Gilbreth, J. Giles, E. Glynn, A. Hall, A. M. Hankin, A. Hansen, D. Hayes, B. Higashi, I. M. Hoffman, B. Horning, J. J. Hout, R. Jacobs, J. Johansen, L. Jones, J. Karcz, T. Klein, P. Lauria, P. Lee, D. Liefer, S. T. Lu, D. Lucchetti, C. Lytle, A. Malm, M. Matheny, B. Mathewson, K. Mayer, D. B. Miller, M. Mills, B. Neyenhuis, L. Nugent, S. Olson, J. Parks, G. N. Price, Z. Price, M. Pugh, A. Ransford, A. P. Reed, C. Roman, M. Rowe, C. Ryan-Anderson, S. Sanders, J. Sedlacek, P. Shevchuk, P. Siegfried, T. Skripka, B. Spaun, R. T. Sprenkle, R. P. Stutz, M. Swallows, R. I. Tobey, A. Tran, T. Tran, E. Vogt, C. Volin, J. Walker, A. M. Zolot, and J. M. Pino, *Phys. Rev. X* **13**, 041052 (2023).
- [11] P. C. Holz, S. Aucher, G. Stocker, M. Valentini, K. Lakhmanskiy, C. Rössler, P. Stampfer, S. Sgouridis, E. Aschauer, Y. Colombe, and R. Blatt, *Advanced Quantum Technologies* **3**, 2000031 (2020).
- [12] S. Jain, J. Alonso, M. Grau, and J. P. Home, *Phys. Rev. X* **10**, 031027 (2020).
- [13] R. Schmied, J. H. Wesenberg, and D. Leibfried, *Phys. Rev. Lett.* **102**, 2 (2009), arXiv:0902.1686.
- [14] F. Hakeberg, P. Kiefer, M. Wittmer, U. Warring, and T. Schaetz, *Phys. Rev. Lett.* **123**, 100504 (2019).
- [15] M. Harlander, R. Lechner, M. Brownnutt, R. Blatt, and W. Hänsel, *Nature* **471**, 200 (2011).
- [16] K. R. Brown, C. Ospelkaus, Y. Colombe, A. C. Wilson, D. Leibfried, and D. J. Wineland, *Nature* **471**, 196 (2011).
- [17] A. C. Wilson, Y. Colombe, K. R. Brown, E. Knill, D. Leibfried, and D. J. Wineland, *Nature* **512**, 57 (2014).
- [18] R. Blatt and D. Wineland, *Nature* **453**, 1008 (2008).
- [19] C. Monroe and J. Kim, *Science* **339**, 1164 (2013).
- [20] D. J. Berkeland, J. D. Miller, J. C. Bergquist, W. M. Itano, and D. J. Wineland, *Journal of Applied Physics* **83**, 5025 (1998).
- [21] R. G. DeVoe, J. Hoffnagle, and R. G. Brewer, *Phys. Rev. A* **39**, 4362 (1989).
- [22] M. Brownnutt, M. Kumph, P. Rabl, and R. Blatt, *Reviews of Modern Physics* **87**, 1419 (2015), arXiv:1409.6572.
- [23] D. T. C. Allcock, L. Guidoni, T. P. Harty, C. J. Ballance, M. G. Blain, A. M. Steane, and D. M. Lucas, *New Journal of Physics* **13**, 123023 (2011).
- [24] R. Dubessy, T. Coudreau, and L. Guidoni, *Phys. Rev. A* **80**, 031402 (2009).
- [25] Q. A. Turchette, Kielpinski, B. E. King, D. Leibfried, D. M. Meekhof, C. J. Myatt, M. A. Rowe, C. A. Sackett, C. S. Wood, W. M. Itano, C. Monroe, and D. J. Wineland, *Phys. Rev. A* **61**, 063418 (2000).
- [26] M. Teller, D. A. Fioretto, P. C. Holz, P. Schindler, V. Messerer, K. Schüppert, Y. Zou, R. Blatt, J. Chiaverini, J. Sage, and T. E. Northup, *Phys. Rev. Lett.* **126**, 230505 (2021).
- [27] D. Kalincev, L. S. Dreissen, A. P. Kulosa, C. H. Yeh, H. A. Fürst, and T. E. Mehlstäubler, *Quantum Science and Technology* **6**, 10.1088/2058-9565/abee99 (2021), arXiv:2012.10336.
- [28] U. Tanaka, M. Nakamura, K. Hayasaka, A. Bautista-Salvador, C. Ospelkaus, and T. E. Mehlstäubler, *Quantum Science and Technology* **6**, 024010 (2021).
- [29] U. Tanaka, K. Suzuki, Y. Ibaraki, and S. Urabe, *Journal of Physics B: Atomic, Molecular and Optical Physics* **47**, 035301 (2014).
- [30] C. A. Sackett, D. Kielpinski, B. E. King, C. Langer, V. Meyer, C. J. Myatt, M. Rowe, Q. A. Turchette, W. M. Itano, D. J. Wineland, and C. Monroe, *Nature* **404**, 256 (2000).
- [31] D. J. Berkeland, J. D. Miller, J. C. Bergquist, W. M. Itano, and D. J. Wineland, *Journal of Applied Physics* **83**, 5025 (1998).
- [32] D. F. V. James, *Applied Physics B* **66**, 181 (1998).
- [33] M. Knoop, in *Physics with Trapped Charged Particles* (Imperial college press, 2014) p. 25–42.
- [34] E. Knill, R. Laflamme, and W. H. Zurek, *Science* **279**, 342 (1998).
- [35] P. Aliferis, D. Gottesman, and J. Preskill, *Quantum Inf. Comput.* **6**, 97 (2006).
- [36] D. Gottesman, *Stabilizer Codes and Quantum Error Correction*, Ph.D. thesis, California Institute of Technology (1997).
- [37] B. M. Terhal, *Rev. Mod. Phys.* **87**, 307 (2015).
- [38] B. Criger and B. Terhal, arXiv preprint arXiv:1604.04062 (2016).
- [39] T. Jochym-O'Connor and R. Laflamme, *Phys. Rev. Lett.*

- 112**, 010505 (2014).
- [40] C. Chamberland, T. Jochym-O'Connor, and R. Laflamme, *Phys. Rev. Lett.* **117**, 010501 (2016).
- [41] C. Chamberland, T. Jochym-O'Connor, and R. Laflamme, *Phys. Rev. A* **95**, 022313 (2017).
- [42] A. Y. Kitaev, *Russian Mathematical Surveys* **52**, 1191 (1997).
- [43] P. Aliferis and J. Preskill, *Phys. Rev. A* **78**, 052331 (2008).
- [44] A. K. Pal, P. Schindler, A. Erhard, Á. Rivas, M.-A. Martin-Delgado, R. Blatt, T. Monz, and M. Müller, *Quantum* **6**, 632 (2022).
- [45] L. Postler, S. Heußen, I. Pogorelov, M. Rispler, T. Feldker, M. Meth, C. D. Marciniak, R. Stricker, M. Ringbauer, R. Blatt, P. Schindler, M. Müller, and T. Monz, *Nature* **605**, 675 (2022).
- [46] L. Postler, F. Butt, I. Pogorelov, C. D. Marciniak, S. Heußen, R. Blatt, P. Schindler, M. Rispler, M. Müller, and T. Monz, arXiv preprint arXiv:2312.09745 (2023).
- [47] C. Ryan-Anderson, N. C. Brown, M. S. Allman, B. Arkin, G. Asa-Attuah, C. Baldwin, J. Berg, J. G. Bohnet, S. Braxton, N. Burdick, J. P. Campora, A. Chernoguzov, J. Esposito, B. Evans, D. Francois, J. P. Gaebler, T. M. Gatterman, J. Gerber, K. Gilmore, D. Gresh, A. Hall, A. Hankin, J. Hostetter, D. Lucchetti, K. Mayer, J. Myers, B. Neyenhuis, J. Santiago, J. Sedlacek, T. Skripka, A. Slattery, R. P. Stutz, J. Tait, R. Tobey, G. Vittorini, J. Walker, and D. Hayes, arXiv preprint 2208.01863 (2022).
- [48] D. Bluvstein, S. J. Evered, A. A. Geim, S. H. Li, H. Zhou, T. Manovitz, S. Ebadi, M. Cain, M. Kalinowski, D. Hangleiter, J. P. Bonilla Ataides, N. Maskara, I. Cong, X. Gao, P. Sales Rodriguez, T. Karolyshyn, G. Semeghini, M. J. Gullans, M. Greiner, V. Vuletić, and M. D. Lukin, *Nature* **626**, 58 (2023).
- [49] A. M. Steane, *Phys. Rev. Lett.* **78**, 2252 (1997).
- [50] C. Chamberland, *New methods in quantum error correction and fault-tolerant quantum computing*, Ph.D. thesis, University of Waterloo (2018).
- [51] D. Bluvstein, S. J. Evered, A. A. Geim, S. H. Li, H. Zhou, T. Manovitz, S. Ebadi, M. Cain, M. Kalinowski, D. Hangleiter, J. P. Bonilla Ataides, N. Maskara, I. Cong, X. Gao, P. Sales Rodriguez, T. Karolyshyn, G. Semeghini, M. J. Gullans, M. Greiner, V. Vuletić, and M. D. Lukin, *Nature* **626**, 58 (2024).
- [52] S. Huang, K. R. Brown, and M. Cetina, arXiv preprint arXiv:2312.10851 (2023).
- [53] S. Heußen, D. F. Locher, and M. Müller, arXiv preprint arXiv:2307.13296 (2023).
- [54] R. S. Gupta, N. Sundaesan, T. Alexander, C. J. Wood, S. T. Merkel, M. B. Healy, M. Hillenbrand, T. Jochym-O'Connor, J. R. Wootton, T. J. Yoder, A. W. Cross, M. Takita, and B. J. Brown, *Nature* **625**, 259 (2024).
- [55] H. Goto, *Scientific Reports* **6**, 19578 (2016).
- [56] C. Chamberland and A. W. Cross, *Quantum* **3**, 143 (2019).
- [57] H. Bombin and M. A. Martin-Delgado, *Phys. Rev. Lett.* **97**, 180501 (2006).
- [58] D. Nigg, M. Müller, E. A. Martinez, P. Schindler, M. Hennrich, T. Monz, M. A. Martin-Delgado, and R. Blatt, *Science* **345**, 302 (2014).